

Interplay between MRI-based axon diameter and myelination estimates in macaque and human brain

Ting Gong^{a*}, Chiara Maffei^a, Evan Dann^a, Hong-Hsi Lee^a, Hansol Lee^a, Jean C. Augustinack^a, Susie Y. Huang^a, Suzanne N. Haber^{b,c}, Anastasia Yendiki^a

- a. Martinos Center for Biomedical Imaging, Massachusetts General Hospital and Harvard Medical School, Charlestown, MA, United States
- b. Department of Pharmacology and Physiology, University of Rochester, Rochester, NY, United States
- c. McLean Hospital, Belmont, MA, United States

*Email: tgong1@mgh.harvard.edu

Abstract

Axon diameter and myelin thickness are closely related microstructural tissue properties that affect the conduction velocity of action potentials in the nervous system. Imaging them non-invasively with MRI-based methods is thus valuable for studying brain microstructure and function. However, the relationship between MRI-based axon diameter and myelination measures has not been investigated across the brain, mainly due to methodological limitations in estimating axon diameters. In recent years, studies using ultra-high gradient strength diffusion MRI (dMRI) have demonstrated improved estimation of axon diameter across white-matter (WM) tracts in the human brain, making such investigations feasible. In this study, we aim to investigate relationships between tissue microstructure properties with MRI-based methods and compare the imaging findings to histological evidence from the literature. We collected dMRI with ultra-high gradient strength and multi-echo spin-echo MRI on ex vivo macaque and human brain samples on a preclinical scanner. From these data, we estimated axon diameter, intra-axonal signal fraction, myelin water fraction (MWF) and aggregate g-ratio and investigated their correlations. We found that the microstructural imaging parameters exhibited consistent patterns across WM tracts and species. In well-myelinated regions, tissue voxels with smaller axons had higher packing density and MWF, while the g-ratio was comparatively independent of axon diameter. The correlation between axon diameter and MWF changed with the level of myelination. We also find that intra-axonal signal fractions and MWF were not consistently correlated when assessed within well-myelinated WM tracts. Overall, the findings suggest that MRI-based axon geometry and myelination measures can provide complementary information about fiber morphology, and the relationships between these measures agree with prior histological evidence. Combining these advanced measures to characterize tissue morphology may help differentiate tissue changes during disease processes such as demyelination versus axonal damage. The regional variations and relationships of microstructural measures in control samples as reported in this study may serve as a point of reference for investigating such tissue changes in disease.

Keywords: axon diameter, myelin, microstructure, brain, MRI

1. Introduction

Axon diameter and myelin thickness are closely related features of tissue microstructure that affect the conduction velocities of neuronal signals (Waxman, 1980) and thus relate to brain function (Caminiti et al., 2013, 2009; Liewald et al., 2014; Tomasi et al., 2012). Relationships between axon diameter and myelin thickness have been shown with microscopic techniques (Hildebrand and Hahn, 1978; Keyserlingk and Schramm, 1984). Non-invasive, MRI-based techniques for estimating these microstructure measures hold great potential as biomarkers in basic and clinical neuroscience. Such methods, however, only provide indirect measurements of axon diameter and myelin density. The sensitivity of such measurements has been evolving with technical advancements. Studying how these advanced, MRI-based estimates vary and relate to each other across the white matter (WM) in the healthy brain, and how these effects correspond to histological evidence, is therefore important for interpreting the findings of future disease applications.

Axon diameter is commonly estimated through microstructure modelling with diffusion weighted (DW) MRI. DW MRI is sensitive to the Brownian motion of water molecules in biological tissue, where the root mean squared displacement is at micrometer length scale at typical observation time, providing unique opportunities to estimate underlying tissue microstructure (Alexander et al., 2019; Novikov et al., 2019). Tissue microstructure is inferred by fitting the DW measurements to biophysical models representing tissue morphology. In representing signals from intra-axonal space, axons are modelled as cylinders with restricted water diffusion in the perpendicular direction (Assaf and Basser, 2005). This was first demonstrated to estimate a gamma distribution of axon diameters in the spinal cord and corpus callosum with the AxCaliber model (Assaf et al., 2008; Barazany et al., 2009). This method requires the DW signals to be measured perpendicular to fiber orientation at different diffusion times and gradient strengths, hence is only applicable to regions with known fiber orientation. The requirement of known fiber orientation is obviated by the ActiveAx method, with orientation invariant acquisition on several diffusion wave vector (q)-shells through an optimal experimental design (Alexander, 2008; Alexander et al., 2010). This method estimates the major fiber orientation and the mean diameter in the model and was later extended to consider dispersion around the fiber orientation (Zhang et al., 2011). Similar to ActiveAx, the TractCaliber method uses a q -shell acquisition from which the major fiber orientation is estimated. It then predicts the signals perpendicular to the fiber orientation and estimates a mean axon diameter from the predicted signals (Huang et al., 2020). Improvements to the signal modelling in the extra-axonal space have also been considered (De Santis et al., 2016). These methods, however, assume a single fiber direction and are not applicable in regions with crossing fibers. As a result, applications of axon diameter estimates have so far focused mostly on areas with coherent fibers, such as the midline of the corpus callosum (Genc et al., 2023; Huang et al., 2019).

Recent developments of axon diameter estimation have focused on using powder-averaged DW signals from the spherical mean technique (Kroenke et al., 2004) to factor out the effect of fiber orientations. These methods have been shown to allow whole-brain WM axon diameter estimation using ultra-high diffusion weighting (b -values) (Andersson et al., 2022; Fan et al., 2020; Pizzolato et al., 2023; Veraart et al., 2020). Such measurements have been made much more practical by human MRI scanners with ultra-strong gradients (Huang et al., 2021, 2014; Jones et al., 2018; McNab et al., 2013). Axon diameter modelling often assumes that the axons are myelinated. However, a range of myelination exists in the

brain and the relationships between these axon diameter estimates and myelination across the brain remain largely unexplored.

Myelin water has very short T2 (~10 ms), making it invisible at typical echo times (>50 ms) in DW MRI (Mackay et al., 1994). Therefore, its quantification is often achieved through other MRI techniques (Mackay and Laule, 2016; Sled, 2017). A well-established method is myelin water imaging through T2 spectrum analysis (Whittall and MacKay, 1989), where the short-T2 signal component is attributed to myelin water. The myelin water fraction (MWF) can then be extracted as a quantitative measure reflecting the amount of myelin wrapped around axons. Currently, spatial variations of myelin content have been reported across the brain (Cercignani et al., 2017; Dean et al., 2016) and the mechanism behind population differences in myelination is an active area of research in neurological conditions, brain development, maturation, and aging (Baum et al., 2022; Cábez et al., 2023; Call and Bergles, 2021; Clark et al., 2021; Grotheer et al., 2022).

Combining axonal and myelination measures is critical for fully characterizing morphological and functional properties of tissue. For example, the fiber g-ratio, defined as the ratio between the inner axon diameter and outer fiber diameter (including myelin sheath), is shown to determine the conduction velocity in histological studies (Castelfranco and Hartline, 2016; Ritchie, 1982; Sanders and Whitteridge, 1946; Waxman, 1980). For MRI-based methods, the tissue aggregate g-ratio has been calculated from myelin volume fraction (MVF) and axon volume fraction (AVF) (Campbell et al., 2018; Mohammadi and Callaghan, 2021; Stikov et al., 2015), which are typically approximated by myelin-sensitive measures and intra-axonal water fractions estimated from DW MRI (Berg et al., 2022), such as NODDI (Zhang et al., 2012). The MR-based g-ratio has been investigated in early brain development (Dean et al., 2016), healthy aging (Bouhrara et al., 2021; Cercignani et al., 2017) and the spinal cord (Duval et al., 2016). However, the direct relationship between axon diameter and myelination and how they associate with g-ratio has not been investigated across the WM.

As the methodology for axon diameter estimation has evolved in recent years, revisiting the relationships of axonal and myelination measures across the brain is of importance. In this study, we estimate axon diameter, intra-axonal signal fraction, MWF and g-ratio with data collected on ex vivo macaque brains and a human brain tissue block with a pre-clinical MRI scanner. In estimating axon diameter, we introduce a multicompartiment model with DW MRI data acquired at multiple b shells and ultra-high b-values that is tailored to ex vivo tissue. We assess the regional variations of these microstructure measures across WM and species and investigate the correlations between them. The relationships reported in this healthy tissue study can serve as a baseline for investigations of changes in these measures in various applications. For example, some applications are characterized by coexisting processes that cause tissue changes, such as axonal damage and demyelination in multiple sclerosis (Huang et al., 2019; Nedjati-Gilani et al., 2017) or axonal growth and myelination in brain development and maturation (Genc et al., 2023). We anticipate that combining axonal geometry and myelination measures will help improve characterization of tissue changes in these applications, facilitated by ultra-high-gradient MRI scanners for in vivo imaging (Huang et al., 2021).

2. Materials & Methods

2.1 Sample preparation

2.1.1 Macaque brains

Two adult male macaques (*Macaca fascicularis*) were anesthetized and perfused with saline followed by a 4% paraformaldehyde/1.5% sucrose solution in 0.1 M PB, pH 7.4. Brains were postfixed overnight and cryoprotected in increasing gradients of sucrose (10%, 20%, and 30%). Surgery and tissue preparation of macaque brain samples were performed at the University of Rochester and details of the procedures are described in previous studies (Grisot et al., 2021; Safadi et al., 2018).

2.1.2 Human tissue block

A tissue block was extracted from the left-brain hemisphere of a 60-year-old female (cause of death: adenocarcinoma of pancreas; postmortem interval: 2 hours) (Williams et al., 2023). The hemisphere was fixed in 10% formalin for at least two months. A 7.5x3.5x1.5 cm tissue block was extracted from a coronal slab in the frontal lobe, containing segments of the anterior limb of the internal capsule and anterior segments of the superior longitudinal fasciculus.

2.2 Data acquisition

We acquired data for the whole macaque brains and human tissue block using a small-bore 4.7 T Bruker BioSpin MRI system equipped with maximum gradient strength of 660 mT/m. The tissue samples were packed in Fomblin (Solvay, Italy) to eliminate background signal.

2.2.1 Diffusion MRI

The DW images were collected using a two-shot, 3D echo-planar imaging sequence at 0.5 mm isotropic resolution. The TR for all scans was 500 ms, with TE of 52 ms for macaque brains and 55 ms for the human brain sample. DW images were collected with b-values up to 43 ms/ μm^2 . For each b-value collected, 12 or 32 gradient directions were uniformly sampled over the hemisphere; one b=0 image is acquired before each b-shell. The separation between diffusion gradient pulses was $\Delta=15$ ms and the duration of diffusion gradient pulses was $\delta=11$ ms. The total acquisition time was 14 hours for a macaque brain and 16 hours for the human tissue block.

For the human tissue block, the whole left hemisphere had previously been scanned on a 3.0 T MRI scanner (0.75 mm isotropic; 12 images at b = 0 and 90 gradient directions at b = 3.8 ms/ μm^2). We used this whole-hemisphere scan here only to perform tractography and locate tracts of interest in the tissue block, as described in a later section.

2.2.2 Myelin water imaging

We collected multi-slice multi-echo (MSME) images using the Carr Purcell Meiboom Gill (CPMG) sequence with slice selective RF pulses to quantify myelin water. The image resolution was 0.5 mm isotropic. The spin-echo images were collected at 20 echo times from 8 - 160 ms with an equal echo spacing of 8 ms and TR of 3000 ms for the macaque samples. Total imaging time was 10 hours. For human samples, the MSME images were collected at 40 echo times from 5-200ms with an equal spacing of 5ms and TR of 2000 ms. Total imaging time was 5 hours.

2.3 Data preprocessing

We first denoised the DW MRI and MSME data, as noise can introduce bias to quantitative parametric mapping. In typically reconstructed and saved magnitude images, the Gaussian noise in the real and

imaginary channel introduces Rician bias to the magnitude signals, which is more prominent for low-SNR data, such as in high b-value DWIs and T2-weighted images with longer echo times in the MSME scan. A previous study has suggested that Rician noise can introduce bias to axon diameter estimation, and extracting real-valued dMRI data with only Gaussian additive noise presented can improve the accuracy of axon diameter estimation (Fan et al., 2020). Denoising images can further improve the SNR, hence the precision of parameter estimation. Other studies have shown that denoising complex images is preferable to magnitude images in both dMRI and myelin water imaging (Does et al., 2019; Manzano Patron et al., 2024).

We evaluated two strategies to reduce bias and noise in the datasets in addition to applying Marchenko-Pastur (MP)-PCA denoising to magnitude images (Veraart et al., 2016b, 2016a). 1. Combining the real and imaginary channel of the complex images for Gaussian noise level estimation; denoising both channels and combining them to obtain magnitude images. 2. Obtaining real-valued images from the complex data as in the background phase filtering procedure introduced in (Eichner et al., 2015; Fan et al., 2020); denoising the real-valued images and discarding the imaginary channel containing mostly background noise. These two denoising strategies require complex MRI datasets.

Following denoising, the DW datasets went through preprocessing steps of Gibbs ringing correction (Kellner et al., 2016), drift check (Vos et al., 2017), eddy current correction (Andersson et al., 2003), gradient orientation correction (Jeurissen et al., 2014), and bias field correction (Tustison et al., 2010) sequentially. We obtained powder-averaged signals, as this approach allows axon diameter estimation at crossing fiber regions (Andersson et al., 2022; Fan et al., 2020; Veraart et al., 2020). This was done by fitting spherical harmonic functions to the DW signals at each b-shell and extracting the zero-order coefficient. We then normalized the signals by the mean b=0 signal prior to axon diameter estimation.

2.4 Microstructural modelling

2.4.1 Tissue model for axon diameter estimation

We fitted the powder-averaged DW signal at each WM voxel to a four-compartment tissue model, including the intra-axonal, extra-cellular, and free water compartments typical for in vivo imaging, with the addition of a dot compartment for ex vivo imaging (Alexander et al., 2010; Panagiotaki et al., 2012). The dot compartment represents immobile water trapped in isotropic structures like cell bodies that does not decay even at very high b-values. This compartment is often ignored for in vivo tissue but can be nonnegligible in fixed ex vivo tissue. We note, however, that signal contribution from the dot compartment has also been demonstrated in vivo using ultra-strong gradients and special diffusion encoding, especially in the cerebellar gray matter (Tax et al., 2020).

The four tissue compartments contribute to the powder-averaged signal decay (normalized to b=0 signal) as a function of b-value as follows:

$$S(b) = f_{ia}S_{ia}(b; D_{\parallel}^{ia}, D_0, d_a) + f_{ec}S_{ec}(b; D_{\perp}^{ec}, D_{\parallel}^{ec}) + f_{csf}S_{csf}(b; D_{csf}) + f_{dot} [1],$$

where the b-value is determined by the diffusion gradient pulse width δ , separation Δ , strength G and gyromagnetic ratio γ as $b = (\gamma\delta G)^2(\Delta - \delta/3)$; f_{ia} , f_{ec} , f_{csf} and f_{dot} are the signal fractions of intra-axonal, extra-cellular, free water and dot compartments, with $f_{ia} + f_{ec} + f_{csf} + f_{dot} = 1$; and S_{ia} , S_{ec}

and S_{csf} are the signal decay functions for the intra-axonal, extra-cellular and free water compartments (their details can be found in Appendix I). Briefly, signal decay of the intra-axonal space (IAS) is modelled by assuming impermeable cylinders with a Gaussian phase distribution approximation perpendicular to the fiber (Van Gelderen et al., 1994), and is parameterized by tissue parameters of intra-axonal parallel diffusivity D_{\parallel}^{ia} , intrinsic diffusivity D_0 and axon diameter d_a . The IAS model is detailed in (Fan et al. 2020)(Andersson et al., 2022), and has been demonstrated to achieve axon diameter estimation at highly aligned fiber and crossing fiber regions in both simulations of realistic fibers segmented from mouse brain (Lee et al., 2020a), vervet monkey brain (Andersson et al., 2022), and human brain (Lee et al., 2024), and in vivo MRI of human brain (Fan et al., 2020). Signal decay from the extra-cellular compartment is modelled as an anisotropic Gaussian parameterized by parallel (D_{\parallel}^{ec}) and perpendicular diffusivity (D_{\perp}^{ec}). The free water compartment is modelled as an isotropic Gaussian parameterized by diffusivity D_{csf} .

2.4.2 Model fitting

Previous studies have adopted some simplifications, reducing the number of parameters to estimate tissue parameters of interest (i.e., d_a and f_{ia}) robustly. Common simplifications include assuming that the intrinsic diffusivity is equal to parallel diffusivity (intra-axonal and extra-cellular), which can be fixed to typical values measured in ex vivo or in vivo tissue. Here, we assume $D_0 = D_{\parallel}^{ia} = D_{\parallel}^{ec}$ and fix the free-water diffusivity D_{csf} to a value typical of ex vivo tissue at room temperature ($2.0 \mu\text{m}^2 / \text{ms}$). However, we estimated the parallel diffusivity from the tissue model. Hence the tissue parameters we fitted were $\theta = (f_{ia}, d_a, D_{\parallel}^{ia}, D_{\perp}^{ec}, f_{csf}, f_{dot})$. We estimate D_{\perp}^{ec} by fitting a fraction of D_{\parallel}^{ia} , such that the former is smaller than the latter.

We used the Markov Chain Monte Carlo (MCMC) method to sample the posterior distribution of modelling parameters. We used uniform priors for diameter $d_a \sim [0.1-10] \mu\text{m}$, parallel diffusivity $D_{\parallel}^{ia} \sim [0.01, 0.9] \mu\text{m}^2 / \text{ms}$, the fraction of extra-cellular perpendicular diffusivity to parallel diffusivity $\sim [0, 1]$ and the noise level $\sigma \sim [0.01-0.1]$. Priors for the signal fractions (f_{ia}, f_{csf}, f_{dot}) were in the range $[0, 1]$, and their sums were constrained in $[0, 1]$, effectively following a Dirichlet distribution. Proposal distributions were Gaussians with small standard deviations. We assumed Gaussian noise, hence the likelihood of measuring powder-averaged DW signal \tilde{S} under modelled signal S at noise level σ is:

$$L(\tilde{S}|S, \sigma) = (2\pi\sigma^2)^{-\frac{n}{2}} \exp\left(-\sum_{i=1}^n \frac{(\tilde{S}(i) - S(i))^2}{2\sigma^2}\right) [2],$$

where S is the prediction from Eq. [1] given acquisition parameters and estimated tissue parameters; n is the number of DW measurements equivalent to the number of non-zero b-values. The log-likelihood ratio was updated using a Metropolis-Hastings sampling algorithm. We used an initial burn-in period of 20,000 iterations and a sampling interval of 100 to gather 500 samples in each run. The estimated tissue parameters were calculated as the mean values of the samples.

When compared to fixing the diffusivity D_{\parallel}^{ia} to typical values ($0.6 \mu\text{m}^2 / \text{ms}$ for ex vivo tissue and $1.7 \mu\text{m}^2 / \text{ms}$ for in vivo tissue), we found that fitting all parameters improves the quality of fit by inspecting the Bayes factor. We also found, however, that this introduces a higher uncertainty of estimated f_{ia} by

inspecting the standard deviations of posterior distribution. We thus repeat the MCMC process twice by first sampling the distributions of all parameters and then, in the second run, fixing D_{\parallel}^{ia} and D_{\perp}^{ec} to their posterior means voxel by voxel and sampling only the distributions of f_{ia} , d_a , f_{csf} and f_{dot} . The second MCMC run gives roughly the same likelihood of measurements and lower parameter uncertainty for f_{ia} and d_a , compared to the first run.

2.4.3 MWF estimation

For myelin water imaging data, we estimated the T2 spectrum from the denoised data using the Julia toolbox for Decomposition and Component Analysis of Exponential Signals (DECAES) (Doucette et al., 2020). We used a non-negative least squares method with calibration to imperfect refocusing pulses due to B1 field inhomogeneity (Prasloski et al., 2012). The spectrum was defined at 100 T2 values logarithmically spaced between 4 ms and 200 ms. From the T2 spectrum, MWF was calculated as the signal fraction from $6\text{ms} < T2 < 15\text{ms}$ for the macaque brains and $6\text{ms} < T2 < 30\text{ms}$ for the human tissue block, after inspecting the spectrum.

2.5 Cross-modal registration

We registered the parameter maps estimated from dMRI into the space of the MSME scan of the same sample, so that axon diameter, intra-axonal fraction and MWF maps were aligned for further analysis. We performed this registration with the advanced normalization tools (ANTs) (Avants et al., 2014) for both macaque brains and human tissue block. We chose one T2-weighted image from the MSME scan that has similar TE to the dMRI scan as the target for this registration. This is because the MSME images are less distorted than the dMRI scan, hence this step also serves as distortion correction for dMRI-derived maps. Before registration, the T2-weighted image from the chosen echo was masked to extract brain voxels and corrected for bias field to remove spatial intensity variation using the N4 bias correction in ANTs (Tustison et al., 2010). The mean $b=0$ image from dMRI was then non-linearly co-registered to the corrected T2-weighted image. The resulting warp field was applied to microstructure parameters estimated in dMRI space.

2.6 G-ratio calculation

After registration, we calculated the g-ratio from the intra-axonal water fraction estimated from the tissue model of diffusion and the MWF estimated from MSME data. The aggregate g-ratio is defined in previous studies (Stikov et al., 2015; West et al., 2015) as:

$$g = \sqrt{\frac{1}{1+MVF/AVF}} \quad [3],$$

where the myelin volume fraction (MVF) can be calculated from myelin sensitive measures and the axon volume fraction (AVF) can be calculated by combining MVF with DW MRI. In our study, we used MWF to quantify myelin; following calibration factors for ex vivo tissue (West et al., 2018), MVF can be calculated from MWF estimates as:

$$MVF = \frac{MWF \times 0.859}{MWF \times 0.384 + 0.475} \quad [4]$$

The AVF was approximated by the absolute intra-axonal water fraction from the compartment model of diffusion as:

$$AVF = (1 - MVF) \times f_{ia} \text{ [5]}$$

Here f_{ia} is the intra-axonal water fraction estimated from the tissue model with DW MRI.

2.7 Tracts and regions definition

We identified the main tract segments that pass through the human tissue block and extracted homologous regions in the macaque brains for cross-species microstructural comparison. For the human sample, tractography and virtual dissection was performed in the whole hemisphere scan. Tract definitions can be found in a previous study (Maffei et al., 2021). We transferred these tract definitions to the block after registering the T2-weighted image from the MSME scan to the b=0 image from the whole hemisphere manually. The identified tracts in the tissue blocks were the superior longitudinal fasciculus (SLF), the anterior commissure (AC), the uncinate fasciculus (UF), and the internal capsule fibers projecting to superior frontal, inferior frontal, and anterior prefrontal cortex (IC1-3). We generated tract ROIs in the block space by applying the inverse affine matrix from the manual registration to the tracts and truncating them. The UF segment in the block was near the intersection with the extreme capsule, which is sometimes defined as the inferior fronto-occipital fasciculus (IFOF).

In the macaque brains, we extracted these similar ROIs from a macaque atlas containing T2 weighted images (Weiss et al., 2021). We registered the T2-weighted image from the atlas to the bias corrected T2-weighted image in the MSME scan, and then applied the warp field to segmentation labels in the atlas, including the SLF, AC, UF and the anterior limb of internal capsule (ALIC). For cross-species comparison of homologous ROIs, we cropped the ROIs in anterior to posterior direction to match the location of the tract segments in the human tissue block. For the macaque brain, we also analyzed the microstructural changes on the corpus callosum (CC), to compare to the findings of previous studies. We use whole brain tractograms to segment the whole CC ROI extracted from the atlas into smaller ROIs, based on cortical termination regions of CC streamlines. These included the rostrum of the genu (connecting the ventral prefrontal cortices), the rest of the genu (connecting the dorsal prefrontal cortices), the four ROIs of the body (connecting the premotor, motor, somatosensory, and parietal cortices), and the splenium (connecting the occipital cortices).

3 Results

3.1 Quality of axon diameter estimation

The denoising method showed a negligible effect on the powder-averaged signal decay curves and therefore axon diameter estimation in our dataset. The evaluation can be found in supplementary materials. Thus, in the following we report parameter estimates from the standard pipeline of denoising magnitude images.

Figure 1 shows the spherical mean signal decay versus b-value and the distribution of MCMC samples from a WM voxel in (a) one macaque sample and (b) the human sample. The four-compartment axon diameter model fitted data from both species well (Fig. 1a and 1b). From the estimated parameters, we found that the human sample had a higher dot signal fraction than the macaque samples, possibly due to differences in fixation methods (immersion vs. perfusion). The parallel diffusivity D_{\parallel}^{ia} is a tissue

factor that affects the resolution limit for axon diameter estimation (Nilsson et al., 2017). The estimated D_{\parallel}^{ia} was around $0.3\sim 0.6 \mu\text{m}^2/\text{ms}$ for our samples, resulting in resolution limits of 1.27 and $1.86 \mu\text{m}$ for parallel and dispersed axons, considering $D_0 = 0.4 \mu\text{m}^2/\text{ms}$ and $\sigma = 0.02$, with the maximal gradient strength $G_{\text{max}} = 660 \text{ mT/m}$ in our protocol.

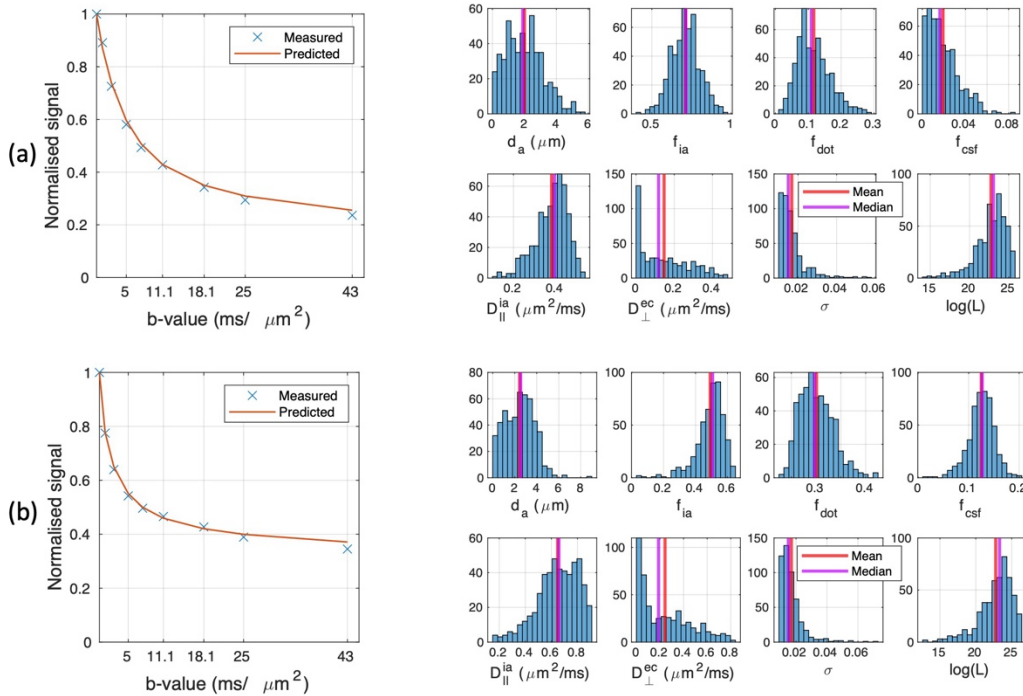


Figure 1. Quality of fitting for axon diameter estimation. The spherical mean signal decay versus b-value and distribution of MCMC samples are shown from a WM voxel of the ALIC for the (a) macaque and (b) human brain sample. The human sample has a higher dot signal fraction.

3.2 Variations of microstructure measures across species

Human sample

Figure 2 shows the location of tracts of interest (TOIs) from the human tissue slab and the distributions of estimated microstructural parameters within each TOI. The SLF, UF and AC have distinct distributions of axon diameters, with AC containing the smallest axons and the UF segments containing the largest ones. The distributions of diameters from segments of the IC were largely overlapping. In all TOIs, the axon diameter estimates were mostly between $\sim 2\text{-}3.5 \mu\text{m}$, and the intra-axonal tissue fractions were between $\sim 0.3\text{-}0.6$. Compared to axon diameter, the MWF had higher variability among TOIs, resulting in variability of the corresponding g-ratios.

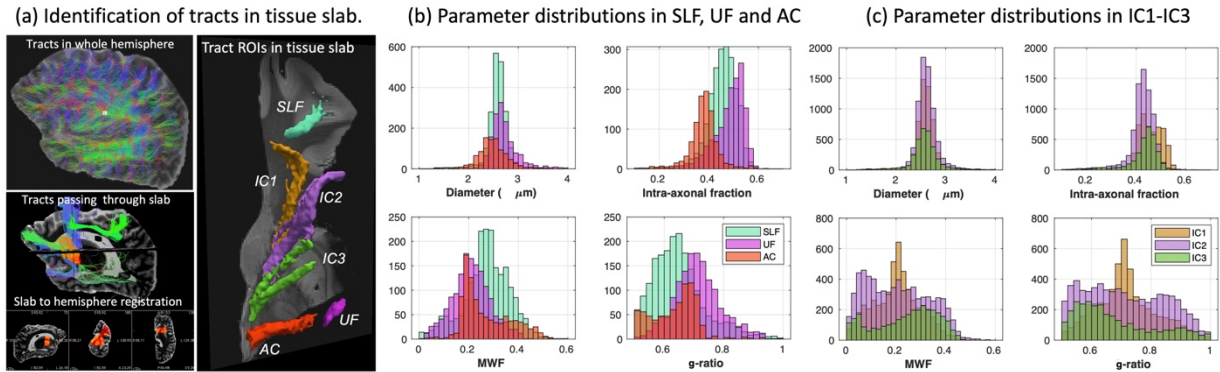


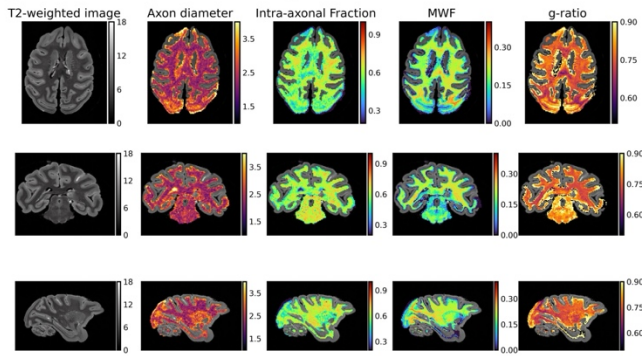
Figure 2. Distributions of parameters in TOIs of the human sample. (a) Pipeline for TOI identification: the whole left hemisphere scan was used for tractography and localization of the tissue block; the tissue block was registered to the whole hemisphere manually and TOIs passing through the block were identified and mapped to the block space. (b-c) Distributions of microstructural parameters in the identified TOIs. SLF = superior longitudinal fasciculus, AC = anterior commissure, UF = uncinate fasciculus, and IC1-3 = internal capsule fibers projecting to superior frontal, inferior frontal, and anterior prefrontal cortex.

Macaque samples

Figure 3 and Figure 4 show microstructure parameter estimates from the macaque brains. Regional differences were not apparent from visual inspection of the parametric maps in a single sample (Figure 3A). As most axon diameter studies have focused on the CC, we show boxplots of parameters in the CC tract segments (Figure 3C). The axon diameter estimates were smaller in the genu than the body of CC, especially in segments of the body connecting motor and somatosensory cortex. The splenium also had smaller axon diameters than the body of CC, exhibiting a low-high-low trend from genu to splenium of CC. Notably, the rostrum of the CC also had larger axon diameter estimates. We observed a reverse trend of intra-axonal fractions among CC tracts. For MWF, CC tracts connecting premotor cortex revealed lower myelin concentrations than the CC rostrum and CC tracts connecting parietal cortex, while all the ROIs were myelinated with MWF around 0.2. This resulted in a reverse trend in g-ratio, which was mostly in the range of 0.7-0.8.

Figure 4 further shows the variations of microstructure parameters from SLF, ALIC, UF in both hemispheres and the AC. The axon diameter had smaller variations than the intra-axonal signal fraction and the MWF. The UF was the least myelinated, hence g-ratios were higher than in other tracts. Among all the association tracts, only the UF showed prominent asymmetry between the left and right hemispheres.

(a) Parameter maps from macaque brain



(b) Corpus callosum (CC) tract segments



(c) Parameter distributions in CC tract segments

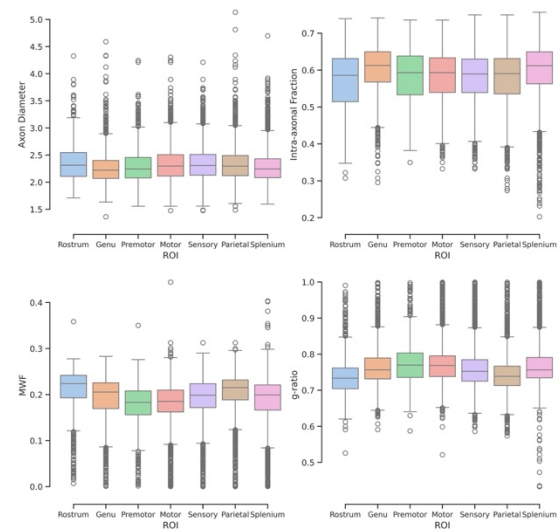


Figure 3. Maps and distributions of microstructure parameters in one of the macaque brains. (a) T2-weighted image overlaid with parameter maps; (b) Tract segments of the corpus callosum (CC). (c) Parameters in CC segments shown as boxplots, where each box and horizontal line represent the interquartile range and median, respectively; the unit for axon diameter is μm .

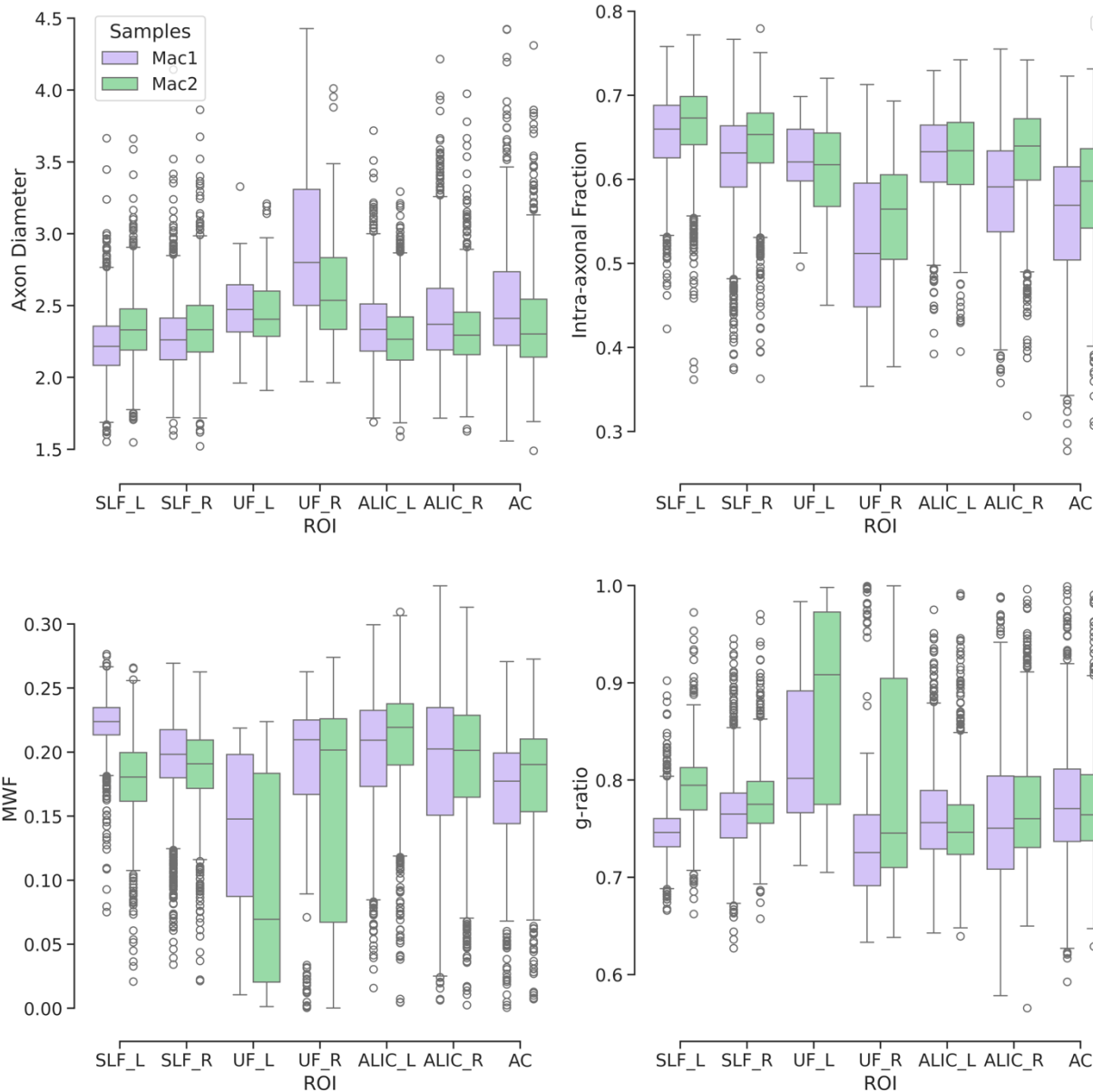


Figure 4. Parameter distributions in ROIs of the macaque brains shown as boxplots. The ROIs include the left (L) and right (R) superior longitudinal fasciculus (SLF), uncinate fasciculus (UF) and anterior limb of the internal capsule (ALIC) and anterior commissure (AC). The unit for axon diameter is μm .

Cross species comparison

Figure 5 shows the comparison of microstructure parameters across species. From parameter distributions, we found consistent variations of microstructure parameters across ROIs in both species. The human tissue had larger axons in the SLF and ALIC and similar axon size in the UF and AC relative to macaque brains. Diameter estimates were mostly between 2-3 μm in both species. The human tissue exhibited higher MWF and thus lower g-ratio in all ROIs (around 0.65) than the macaques (around 0.8). The left UF was the least myelinated and had the highest g-ratio in both species.

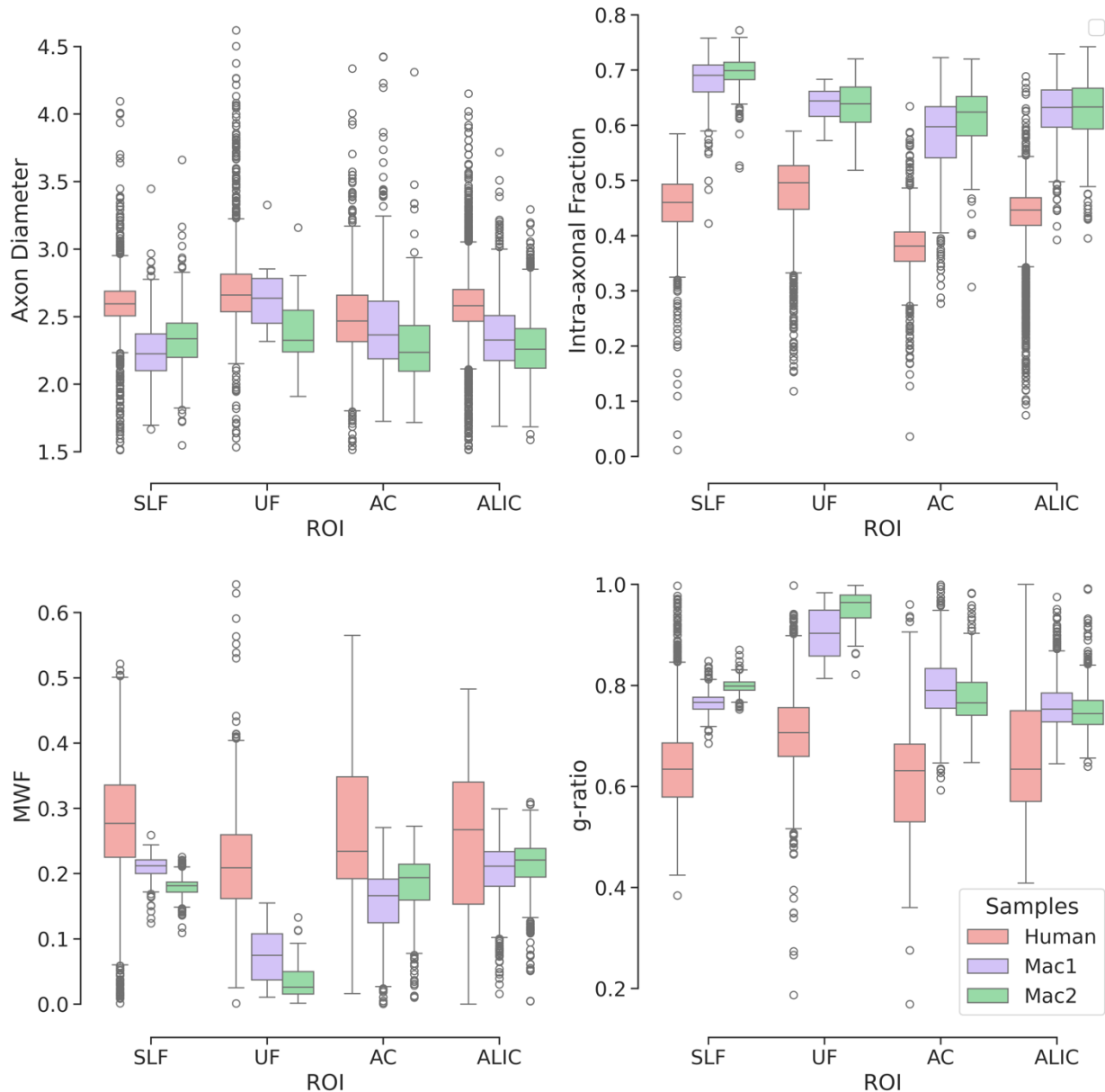


Figure 5. Cross species comparison. The ROIs from the left hemisphere of each macaque brain were cropped to roughly match the location of tract segments in the human tissue block. For the human tissue, IC3 corresponds to ALIC from the macaque brains.

3.3 Correlations between microstructural measures

Figure 6 demonstrates the correlations of microstructure parameters across voxels in each CC TOI of one macaque sample. In well-myelinated CC tracts, the axon diameters showed consistent negative correlations with the intra-axonal fractions and MWF. Correlations between MWF and intra-axonal fraction were not consistent across voxels in each TOI. Regardless of axon diameters, the g-ratio remained stable around 0.8 across all the CC tracts.

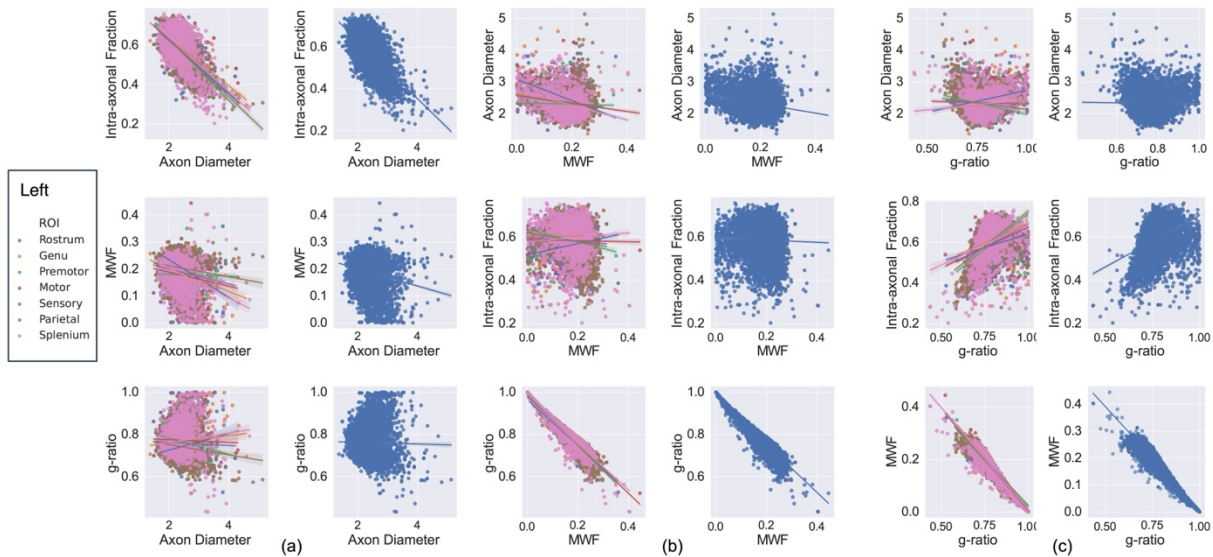


Figure 6. Parameter correlations in well-myelinated CC tracts in the macaque as defined in Figure 3. In (a)-(c), the left column shows scatter plots of voxels and correlations within each ROI and the right column shows correlations considering all the TOIs.

Figure 7 shows the correlations of microstructure parameters in different ROIs from both macaque samples. Consistent with the findings in the CC tracts, the axon diameters were negatively correlated with the intra-axonal fraction and MWF in well-myelinated SLF, ALIC and AC. However, in the less myelinated UF, axon diameters were negatively correlated with intra-axonal fraction but positively correlated with MWF. The correlations between intra-axonal fraction and MWF were not consistent in different ROIs. They were weakly positively correlated when aggregating voxels from all ROIs. G-ratio was not correlated with axon diameter considering different tracts.

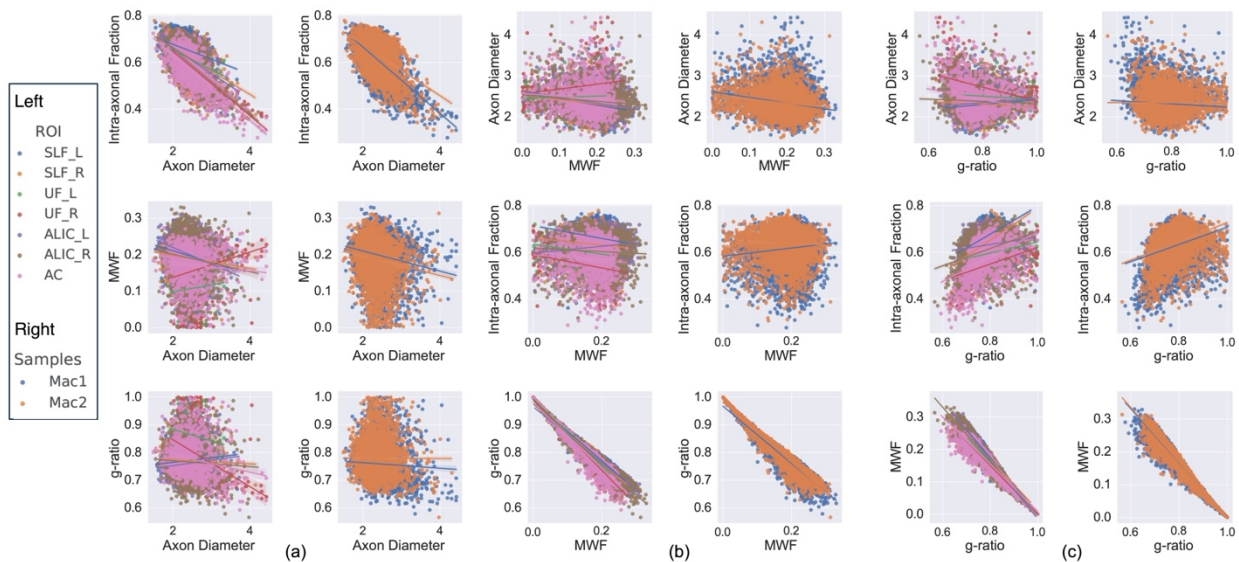


Figure 7. Parameter correlations in tract ROIs in the macaque brains. In (a)-(c), the left column shows scatter plots of voxels and correlations within each ROI from both macaque brains and the right column shows correlations when aggregating all the ROIs for each macaque brain.

Figure 8 considers voxels across all tracts in each sample/species including less myelinated tracts in Figure 4. Consistent with within-tract correlations, axon diameter was negatively correlated with MWF across species. The correlations between axon diameter and intra-axonal fraction are negative in macaque samples while weak in the human sample which also show lower intra-axonal fractions. The correlations between intra-axonal fraction and MWF were positive in the human sample but not consistently so in the macaque brains; these two parameters in the human sample had wider range. The g-ratio, while determined by MWF and axonal fraction, was mostly negatively correlated with MWF as shown from within- and across-tract correlations.

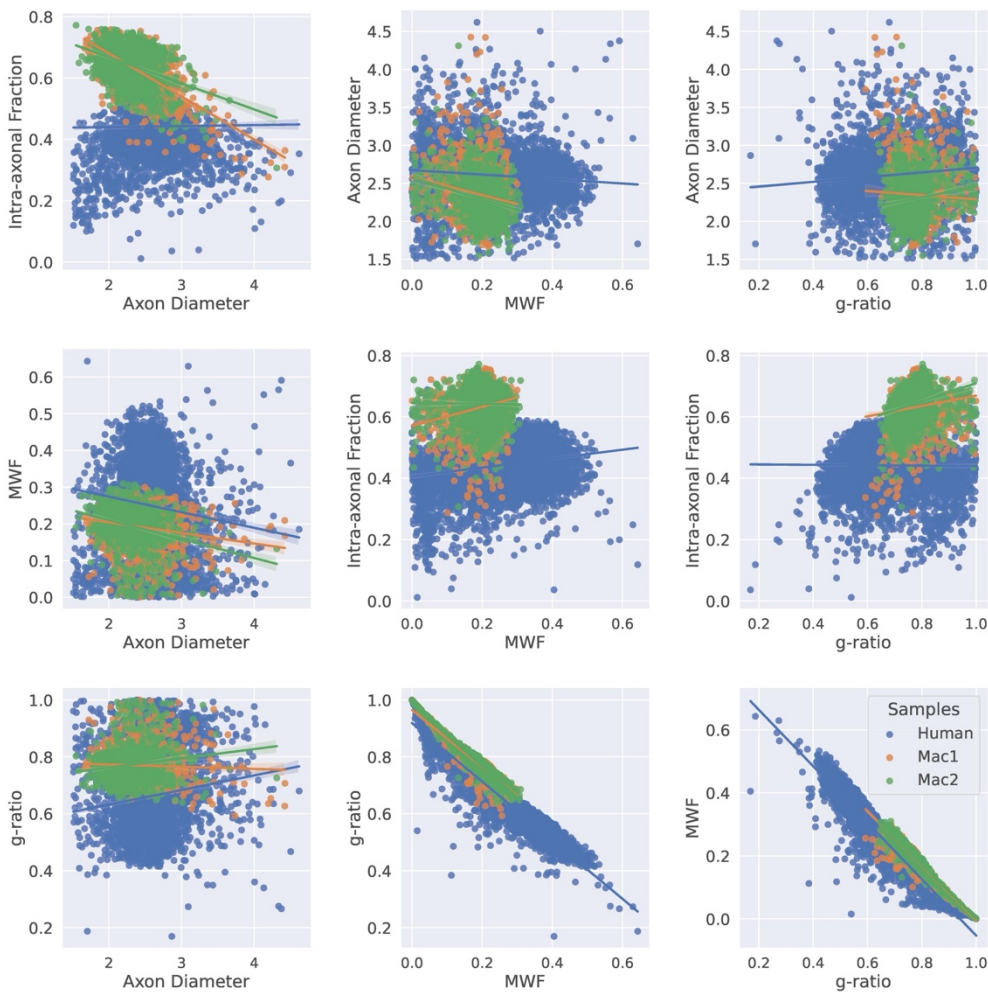


Figure 8. Comparison of parameter correlations between species. The same tract ROIs were included for each sample, (on left) SLF, UF, AC and ALIC – same order as in Figure 5.

4 Discussion

In this study, we investigated the correlations between MRI-based estimates of axon diameter and myelination in WM tracts across human and macaque brain samples. We estimated axon diameter

using a multi-compartment model with the spherical mean technique and quantify myelin content using MWF. We derived a measure of aggregate g-ratio by combining measures derived from dMRI and myelin imaging. We found consistent correlations across species. We discuss the biological implications and methodological considerations below.

4.1 Relationship between axon diameter and myelination

Axon diameter estimates were negatively correlated with intra-axonal signal fraction and MWF across tracts and species in myelinated regions, such that smaller axon estimates were associated with higher intra-axonal signal fraction and myelin concentration. These findings are in accordance with existing histological evidence. First, axons with diameter above 0.2 μm are myelinated in the healthy central nervous system (Hirano and Llena, 1995; Waxman and Bennett, 1972). Axons with smaller diameters are often associated with higher axonal packing density. For example, axons in the genu and splenium of CC appear smaller and denser than in the body of CC in both human and macaque (Aboitiz et al., 1992; Lamantia and Rakic, 1990). While we acknowledge the possibility that the correlation may be an artifact of our multi-compartment model fitting, an almost linear negative correlation between axon diameter and intra-axonal signal fraction is also reported using a different method (De Santis et al., 2016). Second, histological studies show that myelin thickness increases with axon diameter, leading to a relatively constant or increasing g-ratio (Hildebrand and Hahn, 1978; Keyserlingk and Schramm, 1984). Given this constant/increasing g-ratio, tissue voxels with small and densely packed axons will have higher myelin concentration. In our MRI findings, we see the same trends, with relatively stable g-ratios regardless of axon diameter. Furthermore, the axon diameter and myelination estimates originate from different imaging datasets, rendering their correlations more likely to be biologically meaningful.

Surprisingly, while we found correlations between axon diameter and myelination, we did not observe consistent correlations between intra-axonal signal fraction and MWF within well-myelinated CC tracts or across tracts between species. An explanation for this lack of correlation is that our intra-axonal signal fraction could include contributions of restricted diffusion signals from other unmyelinated cylindrical structures, like unmyelinated axons and glia processes, albeit low in the WM. Although the myelin sheath has been considered the main barrier restricting water diffusion perpendicular to axons, early NMR studies also suggest that, even in the absence of myelin, cell membranes alone can introduce diffusion anisotropy (Beaulieu, 2002; Beaulieu and Allen, 1994). Direct evidence is provided by a study using very high-resolution imaging (9 μm) of excised lamprey spinal cord with large and unmyelinated axons (>20 μm), which shows that the diffusion signal is isotropic when measured entirely within a giant axon and anisotropic when measured near axon boundaries (Takahashi et al., 2002). This validates that axon membranes alone cause intra-axonal restriction. Previous studies that demonstrate a positive correlation between intra-axonal signal fraction and MWF (Billiet et al., 2015; De Santis et al., 2014), with exceptions (Qian et al., 2020), were performed under clinical acquisition conditions with much longer diffusion time, where the faster exchange between water in unmyelinated structures and extra-cellular space could have made them indistinguishable. The much shorter diffusion time used in our experiments allows us to gain sensitivity to unmyelinated structures, as it has been demonstrated to separate restricted signal fractions between cell soma and neurites in the gray matter (Ianus et al., 2021; Palombo et al., 2020). However, diseases that affect membrane permeability might change this condition. Thus, combining diffusion measures with MWF is pertinent

in the study of brain disease. Overall, this finding suggests that axonal geometry and MWF can provide complementary information about tissue morphology. This complementary information will be especially helpful in characterizing tissue changes that are caused by coexisting processes, such as axonal growth vs. myelination in healthy brain development, and axonal damage vs. demyelination in diseases such as multiple sclerosis (Yu et al., 2019).

4.2 Estimation of axon diameter

The plausibility of using dMRI to recover axon diameter across the brain has been validated with realistic simulations (Andersson et al., 2022; Lee et al., 2024, 2020a) and histology (Veraart et al., 2020). These studies look at the intra-axonal compartment with very few, ultra-high b-values (≥ 20 ms/ μm^2 for ex vivo tissue). While the dot compartment is often ignored, the signal decay in our data suggests that the dot compartment could be non-negligible, especially in the human sample. We therefore opt to use a multi-compartment modelling framework to model the full signal decay, where we also include lower b-values for extra-cellular and potential CSF compartments. The very strong gradients and short diffusion time in our experiments can minimize bias to diameter estimation from other contributing factors, such as time-dependent diffusion from extra-cellular space (Burcaw et al., 2015; De Santis et al., 2016; Lee et al., 2018), axonal undulation (Brabec et al., 2019; Lee et al., 2024, 2020a) and caliber variation (Lee et al., 2024, 2020a, 2020b).

The range of axon diameter estimates in our study was largely consistent with recent MRI studies. The SLF is reported to contain smaller axons than the IFOF, and the anterior segments of the IFOF have larger axon diameter than the posterior segments (Veraart et al., 2021). Similarly, we report smaller axons in the SLF than the UF/IFOF. We observe the previously reported low-high-low tendency along genu, body, and splenium of CC in our macaque brains, although the between-region differences are small compared to the within-region variability. Interestingly, we also report a distinctly larger axon diameter in the rostrum of the CC, agreeing with a histological finding (Sargon et al., 2003) and an in vivo MRI finding (Veraart et al., 2021).

Several limitations of MR-derived axon diameter estimates have been discussed in previous studies. First, dMRI-estimated axon diameter is representative of the diameter distribution within a tissue voxel but heavily weighted by the tail of the distribution, i.e. larger axons contribute more to the estimate (Burcaw et al., 2015; Neuman, 1974; Sepehrband et al., 2016; Veraart et al., 2020). Variability of diameter estimates thus reflects variability of the tails of diameter distribution across the brain. This could explain the gap between MR-estimated diameter ($>2 \mu\text{m}$) and histological measurements, where most axons are below $1 \mu\text{m}$ with a positive skew in the distributions due to the presence of larger axons. Although it is possible to estimate a distribution of axon diameters with MRI (Assaf et al., 2008), this requires assumptions about the parametric form of this distribution and adds more unknown parameters to the model, reducing its translational potential.

Second, resolution limits for axon diameter estimation might affect regions with aligned and dispersed axons differently. This limit refers to the minimum axon diameter that can be estimated from the dMRI signal given certain experimental conditions and tissue geometries. Thus, a lower limit provides higher resolution for differentiating axons. Using numerical simulation and theoretic prediction (Drobnjak et al., 2016; Lee et al., 2024; Nilsson et al., 2017), previous studies suggest that single diffusion encoding

can achieve lower (better) resolution limit for aligned axons relative to other gradient waveforms. However, it can also result in higher resolution limit in regions with axon dispersion. This can potentially bias the regional variabilities detected with dMRI. However, as the limits with our preclinical and ex vivo settings are generally below 2 μm , this bias should be minimal. Future studies may further experiment with other gradient waveforms, such as oscillating gradients, for coherent resolution limits across the brain, which would be beneficial for in vivo imaging due to the higher diffusivity and resolution limits.

4.3 Estimation of myelin concentration

We have chosen to use myelin water imaging to quantify myelination, as MWF has been shown to be a highly sensitive myelination measure in the WM, when compared to several other methods (Does, 2018; Faizy et al., 2020; Sandrone et al., 2023). We use a relatively mature approach to estimate MWF by acquiring multiple spin-echo images and fitting a T2 spectrum. Several factors will affect the accuracy of the MWF estimation. First, water exchange between myelin water and intra/extra-axonal compartments has been shown to cause changes in the T2 spectrum and therefore lead to underestimating MWF (Harkins et al., 2012). This underestimation is more likely in smaller axons with faster water exchange due to their higher surface-to-volume ratio and thinner myelin sheath (Dortch et al., 2013). However, as we find that smaller axons are associated with higher MWF, water-exchange likely has negligible contribution to our findings. Second, the T2 spectrum fitting is very sensitive to SNR (MacKay et al., 2006); variations in SNR may contribute to the variations of MWF estimates in this study. For future studies to eliminate this fitting bias, a promising technique is the direct visualization of the short-T2 signal component by suppressing signals from other tissue components in the data acquisition (Oh et al., 2013). This technique has recently been accelerated by combination with MR fingerprinting (Liao et al., 2023). Finally, MWF estimates have been shown to be fiber orientation dependent (Birkel et al., 2021). This bias comes from orientation dependent T2, explained by a susceptibility model in myelinated adult brain (Wharton and Bowtell, 2012) and a residual dipolar coupling model in almost unmyelinated newborn brain (Bartels et al., 2022). Calibrating this orientation-dependence bias will be promising in myelin imaging, as has been recently demonstrated in diffusion-informed myelin water imaging (Chan and Marques, 2020) and quantitative susceptibility imaging (Sandgaard et al., 2024).

4.4 Ex vivo tissue

In comparison to in vivo tissue, ex vivo tissue provides several advantages for observing the relationship between microstructure measures. The lower temperature allows us to approach lower resolution limits for estimating axon diameter, as diffusivities are lower in ex vivo tissue (Nilsson et al., 2017). Fixation, shown to decrease membrane permeability (Thelwall et al., 2006), could lower the rate of water exchange, therefore making modelling assumptions, for both axon diameter and myelin imaging, more reasonable. Nevertheless, fixation might also change tissue microstructure properties depending on the quality and method of tissue preservation.

Different fixation methods in macaque vs. human could contribute to the differences observed between species. A previous electron microscopic study has reported a higher axon packing density in macaque than human tissue (Liewald et al., 2014). The explanation for this is the higher fixation quality for macaque brains, which were perfusion fixed, when compared to the longer postmortem interval in

human tissue. This study further explains that the lower packing density does not imply a great loss of fiber populations but is partially due to disintegration of cellular material. This is evidenced by the debris in the space between myelinated fibers in human tissue and an overall similar distribution and mean values of axon diameter in both species. Similarly, an apparent difference that we find between species is the lower intra-axonal signal fractions in the human tissue. Importantly, however, their axon diameters were similar between species, as well as the regional variations of microstructural features.

4.5 Future work

In this study, we used a preclinical system with $G_{\max}=660$ mT/m to investigate relationships between microstructure measures with ex vivo brain samples across species. Validating our findings in vivo will be crucial to further our understanding of these effects. With the development of human MRI scanners with ultra-strong gradients, such as the Connectome 2.0 with $G_{\max}=500$ mT/m (Huang et al., 2021), we will be able to assess axon diameter and myelination in vivo in both healthy and disease populations. In healthy tissue, we have demonstrated between-tract differences of WM microstructure measures. An application of such differences is to inform dMRI tractography (Battocchio et al., 2022; Girard et al., 2017; Schiavi et al., 2022). Future work will explore whether the microstructural differences can help differentiate fiber tracts.

5 Conclusion

Diffusion MRI and MWF measures can provide distinct estimates of axon diameter, axonal fraction, and myelination, supported by consistent regional variability between species. The weak correlations between dMRI metrics and MWF suggest that they provide complementary information about fiber geometry and thus should be combined for thorough microstructure analysis. Considering these correlations in healthy tissue as a baseline will be valuable when studying microstructural changes in disease.

Appendix I

The powder-averaging of DW signals over gradient directions in the spherical mean technique (SMT) yields (Callaghan et al., 1979):

$$S_{smt} = e^{-bD_{\perp}} \sqrt{\frac{\pi}{4b(D_{\parallel}-D_{\perp})}} \operatorname{erf}(\sqrt{b(D_{\parallel}-D_{\perp})}).$$

For the intra-axonal compartment, the perpendicular diffusivity can be used to calculate the axon diameter through Gaussian phase distribution approximation (Neuman, 1974). Therefore, the intra-axonal signal decay is (Fan et al., 2020; Jespersen et al., 2007; Kaden et al., 2016; Van Gelderen et al., 1994):

$$S_{ia}(b(\delta, \Delta, G); D_{\parallel}^{ia}, D_0, d_a) = e^{-bD_{\perp}^{ia}} \sqrt{\frac{\pi}{4b(D_{\parallel}^{ia}-D_{\perp}^{ia})}} \operatorname{erf}(\sqrt{bD_{\parallel}^{ia}-bD_{\perp}^{ia}});$$

$$-bD_{\perp}^{ia} = -2\gamma^2 G^2 \sum_{m=1}^{\infty} \frac{1}{D_0^2 \alpha_m^6 (r_a^2 \alpha_m^2 - 1)} (2D_0 \alpha_m^2 \delta - 2 + 2e^{-D_0 \alpha_m^2 \delta} + 2e^{-D_0 \alpha_m^2 \Delta} - e^{-D_0 \alpha_m^2 (\Delta - \delta)} - e^{-D_0 \alpha_m^2 (\Delta + \delta)}),$$

where $r_a = d_a/2$ is the radius, α_m is the m -th root of $J_1'(\alpha_m r_a) = 0$ and J_1' is the derivative of the first-order Bessel function of the first kind. We calculated the contribution up to $m=10$ in this study.

The anisotropic extra-cellular compartment takes the same form of spherical mean as:

$$S_{ec}(\mathbf{b}; D_{\perp}^{ec}, D_{\parallel}^{ec}) = e^{-bD_{\perp}^{ec}} \sqrt{\frac{\pi}{4b(D_{\parallel}^{ec} - D_{\perp}^{ec})}} \operatorname{erf}\left(\sqrt{b(D_{\parallel}^{ec} - D_{\perp}^{ec})}\right)$$

Finally, the spherical mean of the isotropic free water compartment reduces to:

$$S_{csf}(\mathbf{b}; D_{csf}) = e^{-bD_{csf}}$$

References

- Aboitiz, F., Scheibel, A.B., Fisher, R.S., Zaidel, E., 1992. Fiber composition of the human corpus callosum. *Brain Res* 598, 143–153. [https://doi.org/10.1016/0006-8993\(92\)90178-C](https://doi.org/10.1016/0006-8993(92)90178-C)
- Alexander, D.C., 2008. A General Framework for Experiment Design in Diffusion MRI and Its Application in Measuring Direct Tissue-Microstructure Features. *Magn Reson Med* 60, 439–448. <https://doi.org/10.1002/mrm.21646>
- Alexander, D.C., Dyrby, T.B., Nilsson, M., Zhang, H., 2019. Imaging brain microstructure with diffusion MRI: practicality and applications. *NMR Biomed.* <https://doi.org/10.1002/nbm.3841>
- Alexander, D.C., Hubbard, P.L., Hall, M.G., Moore, E.A., Ptito, M., Parker, G.J.M., Dyrby, T.B., 2010. Orientationally invariant indices of axon diameter and density from diffusion MRI. *Neuroimage* 52, 1374–1389. <https://doi.org/10.1016/j.neuroimage.2010.05.043>
- Andersson, J.L.R., Skare, S., Ashburner, J., 2003. How to correct susceptibility distortions in spin-echo echo-planar images: Application to diffusion tensor imaging. *Neuroimage* 20, 870–888. [https://doi.org/10.1016/S1053-8119\(03\)00336-7](https://doi.org/10.1016/S1053-8119(03)00336-7)
- Andersson, M., Pizzolato, M., Kjer, H.M., Skodborg, K.F., Lundell, H., Dyrby, T.B., 2022. Does powder averaging remove dispersion bias in diffusion MRI diameter estimates within real 3D axonal architectures? *Neuroimage* 248. <https://doi.org/10.1016/j.neuroimage.2021.118718>
- Assaf, Y., Basser, P.J., 2005. Composite hindered and restricted model of diffusion (CHARMED) MR imaging of the human brain. <https://doi.org/10.1016/j.neuroimage.2005.03.042>
- Assaf, Y., Blumenfeld-Katzir, T., Yovel, Y., Basser, P.J., 2008. AxCaliber: A method for measuring axon diameter distribution from diffusion MRI. *Magn Reson Med* 59, 1347–1354. <https://doi.org/10.1002/MRM.21577>
- Avants, B.B., Tustison, N., Johnson, H., 2014. Advanced Normalization Tools (ANTS) Release 2.x.
- Barazany, D., Basser, P.J., Assaf, Y., 2009. In vivo measurement of axon diameter distribution in the corpus callosum of rat brain. *Brain* 132, 1210–1220. <https://doi.org/10.1093/BRAIN/AWP042>

- Bartels, L.M., Doucette, J., Birkl, C., Zhang, Y., Weber, A.M., Rauscher, A., 2022. Orientation dependence of R2 relaxation in the newborn brain. *Neuroimage* 264, 119702. <https://doi.org/10.1016/J.NEUROIMAGE.2022.119702>
- Battocchio, M., Schiavi, S., Descoteaux, M., Daducci, A., 2022. Bundle-o-graphy: improving structural connectivity estimation with adaptive microstructure-informed tractography. *Neuroimage* 263, 119600. <https://doi.org/10.1016/j.neuroimage.2022.119600>
- Baum, G.L., Flournoy, J.C., Glasser, M.F., Harms, M.P., Mair, P., Sanders, A.F.P., Barch, D.M., Buckner, R.L., Bookheimer, S., Dapretto, M., Smith, S., Thomas, K.M., Yacoub, E., Van Essen, D.C., Somerville, L.H., 2022. Graded Variation in T1w/T2w Ratio during Adolescence: Measurement, Caveats, and Implications for Development of Cortical Myelin. *The Journal of Neuroscience* 42, 5681. <https://doi.org/10.1523/JNEUROSCI.2380-21.2022>
- Beaulieu, C., 2002. The basis of anisotropic water diffusion in the nervous system - A technical review. *NMR Biomed* 15, 435–455. <https://doi.org/10.1002/NBM.782>
- Beaulieu, C., Allen, P.S., 1994. Determinants of anisotropic water diffusion in nerves. *Magn Reson Med* 31, 394–400. <https://doi.org/10.1002/MRM.1910310408>
- Berg, R.C., Menegaux, A., Amthor, T., Gilbert, G., Mora, M., Schlaeger, S., Pongratz, V., Lauerer, M., Sorg, C., Doneva, M., Vavasour, I., Mühlau, M., Preibisch, C., 2022. Comparing myelin-sensitive magnetic resonance imaging measures and resulting g-ratios in healthy and multiple sclerosis brains. *Neuroimage* 264. <https://doi.org/10.1016/J.NEUROIMAGE.2022.119750>
- Billiet, T., Vandenbulcke, M., Mädler, B., Peeters, R., Dhollander, T., Zhang, H., Deprez, S., Van den Bergh, B.R.H., Sunaert, S., Emsell, L., 2015. Age-related microstructural differences quantified using myelin water imaging and advanced diffusion MRI. *Neurobiol Aging* 36, 2107–2121. <https://doi.org/10.1016/J.NEUROBIOLAGING.2015.02.029>
- Birkl, C., Doucette, J., Fan, M., Hernández-Torres, E., Rauscher, A., 2021. Myelin water imaging depends on white matter fiber orientation in the human brain. *Magn Reson Med* 85, 2221–2231. <https://doi.org/10.1002/MRM.28543>
- Bouhrara, M., Kim, R.W., Khattar, N., Qian, W., Bergeron, C.M., Melvin, D., Zukley, L.M., Ferrucci, L., Resnick, S.M., Spencer, R.G., 2021. Age-related estimates of aggregate g-ratio of white matter structures assessed using quantitative magnetic resonance neuroimaging. *Hum Brain Mapp* 42, 2362–2373. <https://doi.org/10.1002/HBM.25372>
- Brabec, J., Lasič, S., Nilsson, M., 2019. Time-dependent diffusion in undulating thin fibers: Impact on axon diameter estimation. <https://doi.org/10.1002/nbm.4187>
- Burcaw, L.M., Fieremans, E., Novikov, D.S., 2015. Mesoscopic structure of neuronal tracts from time-dependent diffusion. <https://doi.org/10.1016/j.neuroimage.2015.03.061>
- Cábez, M.B., Vaher, K., York, E.N., Galdi, P., Sullivan, G., Stoye, D.Q., Hall, J., Corrigan, A.E., Quigley, A.J., Waldman, A.D., Bastin, M.E., Thrippleton, M.J., Boardman, J.P., 2023. Characterisation of the neonatal brain using myelin-sensitive magnetisation transfer imaging. *Imaging Neuroscience* 1, 1–17. https://doi.org/10.1162/IMAG_A_00017
- Call, C.L., Bergles, D.E., 2021. Cortical neurons exhibit diverse myelination patterns that scale between mouse brain regions and regenerate after demyelination. *Nature Communications* 2021 12:1 12, 1–15. <https://doi.org/10.1038/s41467-021-25035-2>
- Callaghan, P.T., Jolley, K.W., Lelievre, J., 1979. Diffusion of water in the endosperm tissue of wheat grains as studied by pulsed field gradient nuclear magnetic resonance. *Biophys J* 28, 133. [https://doi.org/10.1016/S0006-3495\(79\)85164-4](https://doi.org/10.1016/S0006-3495(79)85164-4)

- Caminiti, R., Carducci, F., Piervincenzi, C., Battaglia-Mayer, A., Confalone, G., Visco-Comandini, F., Pantano, P., Innocenti, G.M., 2013. Systems/Circuits Diameter, Length, Speed, and Conduction Delay of Callosal Axons in Macaque Monkeys and Humans: Comparing Data from Histology and Magnetic Resonance Imaging Diffusion Tractography. <https://doi.org/10.1523/JNEUROSCI.0761-13.2013>
- Caminiti, R., Ghaziri, H., Galuske, R., Hof, P.R., Innocenti, G.M., 2009. Evolution amplified processing with temporally dispersed slow neuronal connectivity in primates. *Proc Natl Acad Sci U S A* 106, 19551–19556. <https://doi.org/10.1073/PNAS.0907655106>
- Campbell, J.S.W., Leppert, I.R., Narayanan, S., Boudreau, M., Duval, T., Cohen-Adad, J., Pike, G.B., Stikov, N., 2018. Promise and pitfalls of g-ratio estimation with MRI. *Neuroimage*. <https://doi.org/10.1016/j.neuroimage.2017.08.038>
- Castelfranco, A.M., Hartline, D.K., 2016. Evolution of rapid nerve conduction. *Brain Res* 1641, 11–33. <https://doi.org/10.1016/J.BRAINRES.2016.02.015>
- Cercignani, M., Giulietti, G., Dowell, N.G., Gabel, M., Broad, R., Leigh, P.N., Harrison, N.A., Bozzali, M., 2017. Characterizing axonal myelination within the healthy population: a tract-by-tract mapping of effects of age and gender on the fiber g-ratio. *Neurobiol Aging* 49, 109–118. <https://doi.org/10.1016/j.neurobiolaging.2016.09.016>
- Chan, K.S., Marques, J.P., 2020. Multi-compartment relaxometry and diffusion informed myelin water imaging – Promises and challenges of new gradient echo myelin water imaging methods. *Neuroimage* 221, 117159. <https://doi.org/10.1016/J.NEUROIMAGE.2020.117159>
- Clark, I.A., Callaghan, M.F., Weiskopf, N., Maguire, E.A., 2021. The relationship between hippocampal-dependent task performance and hippocampal grey matter myelination and iron content. *Brain Neurosci Adv* 5, 239821282110119. <https://doi.org/10.1177/23982128211011923>
- De Santis, S., Drakesmith, M., Bells, S., Assaf, Y., Jones, D.K., 2014. Why diffusion tensor MRI does well only some of the time: Variance and covariance of white matter tissue microstructure attributes in the living human brain. *Neuroimage* 89, 35. <https://doi.org/10.1016/J.NEUROIMAGE.2013.12.003>
- De Santis, S., Jones, D.K., Roebroek, A., 2016. Including diffusion time dependence in the extra-axonal space improves in vivo estimates of axonal diameter and density in human white matter. *Neuroimage* 130, 91–103. <https://doi.org/10.1016/j.neuroimage.2016.01.047>
- Dean, D.C., O’Muircheartaigh, J., Dirks, H., Travers, B.G., Adluru, N., Alexander, A.L., Deoni, S.C.L., 2016. Mapping an index of the myelin g-ratio in infants using magnetic resonance imaging. *Neuroimage* 132, 225–237. <https://doi.org/10.1016/j.neuroimage.2016.02.040>
- Does, M.D., 2018. Inferring brain tissue composition and microstructure via MR relaxometry. *Neuroimage* 182, 136–148. <https://doi.org/10.1016/J.NEUROIMAGE.2017.12.087>
- Does, M.D., Olesen, J.L., Harkins, K.D., Serradas-Duarte, T., Gochberg, D.F., Jespersen, S.N., Shemesh, N., 2019. Evaluation of principal component analysis image denoising on multi-exponential MRI relaxometry. *Magn Reson Med* 81, 3503–3514. <https://doi.org/10.1002/MRM.27658>
- Dortch, R.D., Harkins, K.D., Juttukonda, M.R., Gore, J.C., Does, M.D., 2013. Characterizing inter-compartmental water exchange in myelinated tissue using relaxation exchange spectroscopy. *Magn Reson Med* 70, 1450–1459. <https://doi.org/10.1002/MRM.24571>
- Doucette, J., Kames, C., Rauscher, A., 2020. DECAES - DEcomposition and Component Analysis of Exponential Signals. *Z Med Phys* 30, 271–278. <https://doi.org/10.1016/J.ZEMEDI.2020.04.001>

- Drobnjak, I., Zhang, H., İlanuş, A., Kaden, E., Alexander, D.C., 2016. PGSE, OGSE, and sensitivity to axon diameter in diffusion MRI: Insight from a simulation study. *Magn Reson Med* 75, 688–700. <https://doi.org/10.1002/MRM.25631>
- Duval, T., Lévy, S., Stikov, N., Campbell, J., Mezer, A., Witzel, T., Keil, B., Smith, V., Wald, L.L., Klawiter, E., Cohen-Adad, J., 2016. g-Ratio weighted imaging of the human spinal cord in vivo. <https://doi.org/10.1016/j.neuroimage.2016.09.018>
- Eichner, C., Cauley, S.F., Cohen-Adad, J., Möller, H.E., Turner, R., Setsompop, K., Wald, L.L., 2015. Real Diffusion-Weighted MRI Enabling True Signal Averaging and Increased Diffusion Contrast. *Neuroimage* 122, 373. <https://doi.org/10.1016/J.NEUROIMAGE.2015.07.074>
- Faizy, T.D., Thaler, C., Broocks, G., Flottmann, F., Leischner, H., Kniep, H., Nawabi, J., Schön, G., Stellmann, J.P., Kemmling, A., Reddy, R., Heit, J.J., Fiehler, J., Kumar, D., Hanning, U., 2020. The Myelin Water Fraction Serves as a Marker for Age-Related Myelin Alterations in the Cerebral White Matter – A Multiparametric MRI Aging Study. *Front Neurosci* 14. <https://doi.org/10.3389/FNINS.2020.00136/FULL>
- Fan, Q., Nummenmaa, A., Witzel, T., Ohringer, N., Tian, Q., Setsompop, K., Klawiter, E.C., Rosen, B.R., Wald, L.L., Huang, S.Y., 2020. Axon diameter index estimation independent of fiber orientation distribution using high-gradient diffusion MRI. *Neuroimage* 222. <https://doi.org/10.1016/j.neuroimage.2020.117197>
- Genc, S., Raven, E.P., Drakesmith, M., Blakemore, S.-J., Jones, D.K., 2023. Novel insights into axon diameter and myelin content in late childhood and adolescence. *Cerebral Cortex* 33, 6435–6448. <https://doi.org/10.1093/cercor/bhac515>
- Girard, G., Daducci, A., Petit, L., Thiran, J.P., Whittingstall, K., Deriche, R., Wassermann, D., Descoteaux, M., 2017. AxTract: Toward microstructure informed tractography. *Hum Brain Mapp* 38, 5485–5500. <https://doi.org/10.1002/HBM.23741>
- Grisot, G., Haber, S.N., Yendiki, A., 2021. Diffusion MRI and anatomic tracing in the same brain reveal common failure modes of tractography. *Neuroimage* 239. <https://doi.org/10.1016/J.NEUROIMAGE.2021.118300>
- Grotheer, M., Rosenke, M., Wu, H., Kular, H., Querdası, F.R., Natu, V.S., Yeatman, J.D., Grill-Spector, K., 2022. White matter myelination during early infancy is linked to spatial gradients and myelin content at birth. *Nature Communications* 2022 13:1 13, 1–12. <https://doi.org/10.1038/s41467-022-28326-4>
- Harkins, K.D., Dula, A.N., Does, M.D., 2012. Effect of intercompartmental water exchange on the apparent myelin water fraction in multiexponential T2 measurements of rat spinal cord. *Magn Reson Med* 67, 793–800. <https://doi.org/10.1002/MRM.23053>
- Hildebrand, C., Hahn, R., 1978. Relation between myelin sheath thickness and axon size in spinal cord white matter of some vertebrate species. *J Neurol Sci* 38, 421–434. [https://doi.org/10.1016/0022-510X\(78\)90147-8](https://doi.org/10.1016/0022-510X(78)90147-8)
- Hirano, A., Lena, J.F., 1995. Morphology of central nervous system axons. *The Axon: Structure, Function and Pathophysiology*. <https://doi.org/10.1093/ACPROF:OSO/9780195082937.003.0003>
- Huang, S.Y., Fan, Q., Machado, N., Eloyan, A., Bireley, J.D., Russo, A.W., Tobyne, S.M., Patel, K.R., Brewer, K., Rapaport, S.F., Nummenmaa, A., Witzel, T., Sherman, J.C., Wald, L.L., Klawiter, E.C., 2019. Corpus callosum axon diameter relates to cognitive impairment in multiple sclerosis. *Ann Clin Transl Neurol* 6, 882–892. <https://doi.org/10.1002/ACN3.760>

- Huang, S.Y., Nummenmaa, A., Witzel, T., Duval, T., Cohen-Adad, J., Wald, L.L., McNab, J.A., 2014. The impact of gradient strength on in vivo diffusion MRI estimates of axon diameter. <https://doi.org/10.1016/j.neuroimage.2014.12.008>
- Huang, S.Y., Tian, Q., Fan, Q., Witzel, T., Wichtmann, B., McNab, J.A., Daniel Bireley, J., Machado, N., Klawiter, E.C., Mekkaoui, C., Wald, L.L., Nummenmaa, A., 2020. High-gradient diffusion MRI reveals distinct estimates of axon diameter index within different white matter tracts in the in vivo human brain. *Brain Struct Funct* 225, 1277–1291. <https://doi.org/10.1007/s00429-019-01961-2>
- Huang, S.Y., Witzel, T., Keil, B., Scholz, A., Davids, M., Dietz, P., Rummert, E., Ramb, R., Kirsch, J.E., Yendiki, A., Fan, Q., Tian, Q., Ramos-Llordén, G., Lee, H.H., Nummenmaa, A., Bilgic, B., Setsompop, K., Wang, F., Avram, A. V., Komlosh, M., Benjamini, D., Magdoom, K.N., Pathak, S., Schneider, W., Novikov, D.S., Fieremans, E., Tounekti, S., Mekkaoui, C., Augustinack, J., Berger, D., Shapson-Coe, A., Lichtman, J., Basser, P.J., Wald, L.L., Rosen, B.R., 2021. Connectome 2.0: Developing the next-generation ultra-high gradient strength human MRI scanner for bridging studies of the micro-, meso- and macro-connectome. *Neuroimage* 243. <https://doi.org/10.1016/J.NEUROIMAGE.2021.118530>
- Ianus, A., Alexander, D.C., Zhang, H., Palombo, M., 2021. Mapping complex cell morphology in the grey matter with double diffusion encoding MR: A simulation study. *Neuroimage* 241. <https://doi.org/10.1016/J.NEUROIMAGE.2021.118424>
- Jespersen, S.N., Kroenke, C.D., Østergaard, L., Ackerman, J.J.H., Yablonskiy, D.A., 2007. Modeling dendrite density from magnetic resonance diffusion measurements. *Neuroimage* 34, 1473–1486. <https://doi.org/10.1016/j.neuroimage.2006.10.037>
- Jeurissen, B., Leemans, A., Sijbers, J., 2014. Automated correction of improperly rotated diffusion gradient orientations in diffusion weighted MRI. *Med Image Anal* 18, 953–962. <https://doi.org/10.1016/J.MEDIA.2014.05.012>
- Jones, D., Alexander, D., Bowtell, R., Cercignani, M., Dell, F., McHugh, D., Miller, K., Palombo, M., Parker, G., Rudrapatna, U., Tax, C., Cambridge, in, 2018. Microstructural imaging of the human brain with a “super-scanner”: 10 key advantages of ultra-strong gradients for diffusion MRI. <https://doi.org/10.1016/j.neuroimage.2018.05.047>
- Kaden, E., Kelm, N.D., Carson, R.P., Does, M.D., Alexander, D.C., 2016. Multi-compartment microscopic diffusion imaging. *Neuroimage* 139, 346–359. <https://doi.org/10.1016/J.NEUROIMAGE.2016.06.002>
- Kellner, E., Dhital, B., Kiselev, V.G., Reisert, M., 2016. Gibbs-ringing artifact removal based on local subvoxel-shifts. *Magn Reson Med* 76. <https://doi.org/10.1002/mrm.26054>
- Keyserlingk, D.G. von, Schramm, U., 1984. Diameter of axons and thickness of myelin sheaths of the pyramidal tract fibres in the adult human medullary pyramid. *Anat Anz*.
- Kroenke, C.D., Ackerman, J.J.H., Yablonskiy, D.A., 2004. On the nature of the NAA diffusion attenuated MR signal in the central nervous system. *Magn Reson Med* 52, 1052–1059. <https://doi.org/10.1002/MRM.20260>
- Lamantia, A. -S, Rakic, P., 1990. Cytological and quantitative characteristics of four cerebral commissures in the rhesus monkey. *Journal of Comparative Neurology* 291, 520–537. <https://doi.org/10.1002/CNE.902910404>

- Lee, H.H., Fieremans, E., Novikov, D.S., 2018. What dominates the time dependence of diffusion transverse to axons: Intra- or extra-axonal water? *Neuroimage* 182, 500–510. <https://doi.org/10.1016/J.NEUROIMAGE.2017.12.038>
- Lee, H.H., Jespersen, S.N., Fieremans, E., Novikov, D.S., 2020a. The impact of realistic axonal shape on axon diameter estimation using diffusion MRI. *Neuroimage* 223, 117228. <https://doi.org/10.1016/J.NEUROIMAGE.2020.117228>
- Lee, H.H., Papaioannou, A., Kim, S.L., Novikov, D.S., Fieremans, E., 2020b. A time-dependent diffusion MRI signature of axon caliber variations and beading. *Communications Biology* 2020 3:1 3, 1–13. <https://doi.org/10.1038/s42003-020-1050-x>
- Lee, H.H., Tian, Q., Sheft, M., Coronado-Leija, R., Ramos-Llorden, G., Abdollahzadeh, A., Fieremans, E., Novikov, D.S., Huang, S.Y., 2024. The effects of axonal beading and undulation on axonal diameter estimation from diffusion MRI: Insights from simulations in human axons segmented from three-dimensional electron microscopy. *NMR Biomed.* <https://doi.org/10.1002/NBM.5087>
- Liao, C., Cao, X., Iyer, S.S., Schauman, S., Zhou, Z., Yan, X., Chen, Q., Li, Z., Wang, N., Gong, T., Wu, Z., He, H., Zhong, J., Yang, Y., Kerr, A., Grill-Spector, K., Setsompop, K., 2023. High-resolution myelin-water fraction and quantitative relaxation mapping using 3D ViSta-MR fingerprinting. *Magn Reson Med.* <https://doi.org/10.1002/MRM.29990>
- Liewald, Daniel, Miller, Robert, Logothetis, N., Wagner, Hans-Joachim, Schüz, Almut, Liewald, D, Logothetis, N, Schüz, A, Miller, R, Wagner, H.-J, 2014. Distribution of axon diameters in cortical white matter: an electron-microscopic study on three human brains and a macaque. *Biol Cybern* 108, 541–557. <https://doi.org/10.1007/s00422-014-0626-2>
- MacKay, A., Laule, C., Vavasour, I., Bjarnason, T., Kolind, S., Mädler, B., 2006. Insights into brain microstructure from the T2 distribution. *Magn Reson Imaging.* <https://doi.org/10.1016/j.mri.2005.12.037>
- Mackay, A., Whittall, K., Adler, J., Li, D., Paty, D., Graeb, D., 1994. In vivo visualization of myelin water in brain by magnetic resonance. *Magn Reson Med* 31, 673–677. <https://doi.org/10.1002/MRM.1910310614>
- Mackay, A.L., Laule, C., 2016. Magnetic Resonance of Myelin Water: An in vivo Marker for Myelin. *Brain Plasticity* 2, 71–91. <https://doi.org/10.3233/BPL-160033>
- Maffei, C., Lee, C., Planich, M., Ramprasad, M., Ravi, N., Trainor, D., Urban, Z., Kim, M., Jones, R.J., Henin, A., Hofmann, S.G., Pizzagalli, D.A., Auerbach, R.P., Gabrieli, J.D.E., Whitfield-Gabrieli, S., Greve, D.N., Haber, S.N., Yendiki, A., 2021. Using diffusion MRI data acquired with ultra-high gradient strength to improve tractography in routine-quality data. *Neuroimage* 245, 118706. <https://doi.org/10.1016/j.neuroimage.2021.118706>
- Manzano Patron, J.P., Moeller, S., Andersson, J.L.R., Ugurbil, K., Yacoub, E., Sotiropoulos, S.N., 2024. Denoising diffusion MRI: Considerations and implications for analysis. *Imaging Neuroscience* 2, 1–29. https://doi.org/10.1162/IMAG_A_00060
- Mcnab, J.A., Edlow, B.L., Witzel, T., Huang, S.Y., Bhat, H., Heberlein, K., Feiweier, T., Liu, K., Keil, B., Cohen-Adad, J., Dylan Tisdall, M., Folkerth, R.D., Kinney, H.C., Wald, L.L., 2013. The Human Connectome Project and Beyond: Initial Applications of 300 mT/m Gradients. <https://doi.org/10.1016/j.neuroimage.2013.05.074>
- Mohammadi, S., Callaghan, M.F., 2021. Towards in vivo g-ratio mapping using MRI: Unifying myelin and diffusion imaging. *J Neurosci Methods* 348, 108990. <https://doi.org/10.1016/J.JNEUMETH.2020.108990>

- Nedjati-Gilani, G.L., Schneider, T., Hall, M.G., Cawley, N., Hill, I., Ciccarelli, O., Drobnyak, I., Wheeler-Kingshott, C.A.M.G., Alexander, D.C., 2017. Machine learning based compartment models with permeability for white matter microstructure imaging. *Neuroimage* 150, 119–135. <https://doi.org/10.1016/J.NEUROIMAGE.2017.02.013>
- Neuman, C.H., 1974. Spin echo of spins diffusing in a bounded medium. *J Chem Phys* 4508–4511. <https://doi.org/10.1063/1.1680931>
- Nilsson, M., Lasič, S., Drobnyak, I., Topgaard, D., Westin, C.F., 2017. Resolution limit of cylinder diameter estimation by diffusion MRI: The impact of gradient waveform and orientation dispersion. *NMR Biomed* 30. <https://doi.org/10.1002/NBM.3711>
- Novikov, D.S., Fieremans, E., Jespersen, S.N., Kiselev, V.G., 2019. Quantifying brain microstructure with diffusion MRI: Theory and parameter estimation. *NMR Biomed*. <https://doi.org/10.1002/nbm.3998>
- Oh, S.H., Bilello, M., Schindler, M., Markowitz, C.E., Detre, J.A., Lee, J., 2013. Direct visualization of short transverse relaxation time component (ViSta). *Neuroimage* 83, 485–492. <https://doi.org/10.1016/J.NEUROIMAGE.2013.06.047>
- Palombo, M., Ianus, A., Guerreri, M., Nunes, D., Alexander, D.C., Shemesh, N., Zhang, H., 2020. SANDI: A compartment-based model for non-invasive apparent soma and neurite imaging by diffusion MRI. *Neuroimage* 215. <https://doi.org/10.1016/j.neuroimage.2020.116835>
- Panagiotaki, E., Schneider, T., Siow, B., Hall, M.G., Lythgoe, M.F., Alexander, D.C., 2012. Compartment models of the diffusion MR signal in brain white matter: A taxonomy and comparison. *Neuroimage* 59, 2241–2254. <https://doi.org/10.1016/j.neuroimage.2011.09.081>
- Pizzolato, M., Canales-Rodríguez, E.J., Andersson, M., Dyrby, T.B., 2023. Axial and radial axonal diffusivities and radii from single encoding strongly diffusion-weighted MRI. *Med Image Anal* 86. <https://doi.org/10.1016/J.MEDIA.2023.102767>
- Prasloski, T., Mädler, B., Xiang, Q.S., MacKay, A., Jones, C., 2012. Applications of stimulated echo correction to multicomponent T2 analysis. *Magn Reson Med* 67, 1803–1814. <https://doi.org/10.1002/MRM.23157>
- Qian, W., Khattar, N., Cortina, L.E., Spencer, R.G., Bouhrara, M., 2020. Nonlinear associations of neurite density and myelin content with age revealed using multicomponent diffusion and relaxometry magnetic resonance imaging. *Neuroimage* 223, 117369. <https://doi.org/10.1016/J.NEUROIMAGE.2020.117369>
- Ritchie, J.M., 1982. On the relation between fibre diameter and conduction velocity in myelinated nerve fibres. *Proceedings of the Royal Society of London - Biological Sciences* 217, 29–35. <https://doi.org/10.1098/RSPB.1982.0092>
- Safadi, Z., Grisot, G., Jbabdi, S., Behrens, T.E., Heilbronner, S.R., McLaughlin, N.C.R., Mandeville, J., Versace, A., Phillips, M.L., Lehman, J.F., Yendiki, A., Haber, S.N., 2018. Functional Segmentation of the Anterior Limb of the Internal Capsule: Linking White Matter Abnormalities to Specific Connections. *The Journal of Neuroscience* 38, 2106. <https://doi.org/10.1523/JNEUROSCI.2335-17.2017>
- Sanders, F.K., Whitteridge, D., 1946. CONDUCTION VELOCITY AND MYELIN THICKNESS IN REGENERATING NERVE FIBRES. *J. Physiol* 05, 52–74.
- Sandgaard, A.D., Kiselev, V.G., Henriques, R.N., Shemesh, N., Jespersen, S.N., 2024. Incorporating the effect of white matter microstructure in the estimation of magnetic susceptibility in ex vivo mouse brain. *Magn Reson Med* 91, 699–715. <https://doi.org/10.1002/MRM.29867>

- Sandrone, S., Aiello, M., Cavaliere, C., Michel Thiebaut De Schotten, ·, Reimann, K., Troakes, C., Bodi, I., Lacerda, · Luis, Monti, S., Murphy, D., Geyer, S., Catani, M., Dell'acqua, F., Dell', F., 2023. Mapping myelin in white matter with T1-weighted/T2-weighted maps: discrepancy with histology and other myelin MRI measures. *Brain Struct Funct* 228, 525–535. <https://doi.org/10.1007/s00429-022-02600-z>
- Sargon, M.F., Mas, N., Şenan, S., Özdemir, B., Çelik, H.H., Cumhur, M., 2003. Quantitative analysis of myelinated axons of commissural fibers in the rat brain. *Anat Histol Embryol* 32, 141–144. <https://doi.org/10.1046/J.1439-0264.2003.00446.X>
- Schiavi, S., Lu, P.J., Weigel, M., Lutti, A., Jones, D.K., Kappos, L., Granziera, C., Daducci, A., 2022. Bundle myelin fraction (BMF) mapping of different white matter connections using microstructure informed tractography. *Neuroimage* 249. <https://doi.org/10.1016/j.neuroimage.2022.118922>
- Sepehrband, F., Alexander, D.C., Kurniawan, N.D., Reutens, D.C., Yang, Z., 2016. Towards higher sensitivity and stability of axon diameter estimation with diffusion-weighted MRI. *NMR Biomed* 29, 293–308. <https://doi.org/10.1002/NBM.3462>
- Sled, J.G., 2017. Modelling and interpretation of magnetization transfer imaging in the brain. <https://doi.org/10.1016/j.neuroimage.2017.11.065>
- Stikov, N., Campbell, J.S.W., Stroh, T., Lavelée, M., Frey, S., Novek, J., Nuara, S., Ho, M.K., Bedell, B.J., Dougherty, R.F., Leppert, I.R., Boudreau, M., Narayanan, S., Duval, T., Cohen-Adad, J., Picard, P.A., Gasecka, A., Côté, D., Pike, G.B., 2015. In vivo histology of the myelin g-ratio with magnetic resonance imaging. *Neuroimage* 118, 397–405. <https://doi.org/10.1016/j.neuroimage.2015.05.023>
- Takahashi, M., Hackney, D.B., Zhang, G., Wehrli, S.L., Wright, A.C., O'Brien, W.T., Uematsu, H., Wehrli, F.W., Seizer, M.E., 2002. Magnetic resonance microimaging of intraaxonal water diffusion in live excised lamprey spinal cord. *Proc Natl Acad Sci U S A* 99, 16192. <https://doi.org/10.1073/PNAS.252249999>
- Tax, C.M.W., Szczepankiewicz, F., Nilsson, M., Jones, D.K., 2020. The dot-compartment revealed? Diffusion MRI with ultra-strong gradients and spherical tensor encoding in the living human brain. *Neuroimage* 210. <https://doi.org/10.1016/j.neuroimage.2020.116534>
- Thelwall, P.E., Shepherd, T.M., Stanis, G.J., Blackband, S.J., 2006. Effects of temperature and aldehyde fixation on tissue water diffusion properties, studied in an erythrocyte ghost tissue model. *Magn Reson Med* 56, 282–289. <https://doi.org/10.1002/mrm.20962>
- Tomasi, S., Caminiti, R., Innocenti, G.M., 2012. Areal Differences in Diameter and Length of Corticofugal Projections. *Cerebral Cortex* 22, 1463–1472. <https://doi.org/10.1093/cercor/bhs011>
- Tustison, N.J., Avants, B.B., Cook, P.A., Zheng, Y., Egan, A., Yushkevich, P.A., Gee, J.C., 2010. N4ITK: Improved N3 bias correction. *IEEE Trans Med Imaging* 29, 1310–1320. <https://doi.org/10.1109/TMI.2010.2046908>
- Van Gelderen, P., Des Pres, D., Van Zijl, P.C.M., Moonen, C.T.W., 1994. Evaluation of Restricted Diffusion in Cylinders. Phosphocreatine in Rabbit Leg Muscle. *J Magn Reson B* 103, 255–260. <https://doi.org/10.1006/JMRB.1994.1038>
- Veraart, J., Fieremans, E., Novikov, D.S., 2016a. Diffusion MRI noise mapping using random matrix theory. *Magn Reson Med* 76, 1582–1593. <https://doi.org/10.1002/mrm.26059>
- Veraart, J., Novikov, D.S., Christiaens, D., Ades-aron, B., Sijbers, J., Fieremans, E., 2016b. Denoising of diffusion MRI using random matrix theory. *Neuroimage* 142. <https://doi.org/10.1016/j.neuroimage.2016.08.016>

- Veraart, J., Nunes, D., Rudrapatna, U., Fieremans, E., Jones, D.K., Novikov, D.S., Shemesh, N., 2020. Noninvasive quantification of axon radii using diffusion MRI. *Elife* 9. <https://doi.org/10.7554/eLife.49855>
- Veraart, J., Raven, E.P., Edwards, L.J., Weiskopf, N., Jones, D.K., 2021. The variability of MR axon radii estimates in the human white matter. *Hum Brain Mapp* 42, 2201–2213. <https://doi.org/10.1002/HBM.25359>
- Vos, S.B., Tax, C.M.W., Luijten, P.R., Ourselin, S., Leemans, A., Froeling, M., 2017. The importance of correcting for signal drift in diffusion MRI. *Magn Reson Med* 77. <https://doi.org/10.1002/mrm.26124>
- Waxman, S.G., 1980. Determinants of conduction velocity in myelinated nerve fibers. *Muscle Nerve* 3, 141–150. <https://doi.org/10.1002/MUS.880030207>
- Waxman, S.G., Bennett, M.V.I., 1972. Relative Conduction Velocities of Small Myelinated and Non-myelinated Fibres in the Central Nervous System. *Nature New Biology* 1972 238:85 238, 217–219. <https://doi.org/10.1038/newbio238217a0>
- Weiss, A.R., Liu, Z., Wang, X., Liguore, W.A., Kroenke, C.D., McBride, J.L., 2021. The macaque brain ONPRC18 template with combined gray and white matter labelmap for multimodal neuroimaging studies of Nonhuman Primates. *Neuroimage* 225. <https://doi.org/10.1016/j.neuroimage.2020.117517>
- West, K.L., Kelm, N.D., Carson, R.P., Does, M.D., 2015. A revised model for estimating g-ratio from MRI ☆. <https://doi.org/10.1016/j.neuroimage.2015.08.017>
- West, K.L., Kelm, N.D., Carson, R.P., Gochberg, D.F., Ess, K.C., Does, M.D., 2018. Myelin volume fraction imaging with MRI. *Neuroimage* 182, 511–521. <https://doi.org/10.1016/J.NEUROIMAGE.2016.12.067>
- Wharton, S., Bowtell, R., 2012. Fiber orientation-dependent white matter contrast in gradient echo MRI. *Proc Natl Acad Sci U S A* 109, 18559–18564. https://doi.org/10.1073/PNAS.1211075109/SUPPL_FILE/PNAS.201211075SI.PDF
- Whittall, K.P., MacKay, A.L., 1989. Quantitative interpretation of NMR relaxation data. *Journal of Magnetic Resonance (1969)* 84, 134–152. [https://doi.org/10.1016/0022-2364\(89\)90011-5](https://doi.org/10.1016/0022-2364(89)90011-5)
- Williams, E.M., Rosenblum, E.W., Pihlstrom, N., Llamas-Rodríguez, J., Champion, S., Frosch, M.P., Augustinack, J.C., 2023. Pentad: A reproducible cytoarchitectonic protocol and its application to parcellation of the human hippocampus. *Front Neuroanat* 17, 1114757. <https://doi.org/10.3389/FNANA.2023.1114757/BIBTEX>
- Yu, F., Fan, Q., Tian, Q., Ngamsombat, C., Machado, N., Bireley, J.D., Russo, A.W., Nummenmaa, A., Witzel, T., Wald, L.L., Klawiter, E.C., Huang, S.Y., 2019. Imaging G-Ratio in Multiple Sclerosis Using High-Gradient Diffusion MRI and Macromolecular Tissue Volume. *American Journal of Neuroradiology* 40, 1871–1877. <https://doi.org/10.3174/AJNR.A6283>
- Zhang, H., Hubbard, P.L., Parker, G.J.M., Alexander, D.C., 2011. Axon diameter mapping in the presence of orientation dispersion with diffusion MRI. *Neuroimage* 56, 1301–1315. <https://doi.org/10.1016/j.neuroimage.2011.01.084>
- Zhang, H., Schneider, T., Wheeler-Kingshott, C.A., Alexander, D.C., 2012. NODDI: Practical in vivo neurite orientation dispersion and density imaging of the human brain. *Neuroimage* 61, 1000–1016. <https://doi.org/10.1016/j.neuroimage.2012.03.072>

Ethics

All experiments on macaques were performed in accordance with the Institute of Laboratory Animal Resources Guide for the Care and Use of Laboratory Animals and approved by the University of Rochester Committee on Animal Resources. All experiments involving human tissue were approved by the Institutional Review Board at Massachusetts General Hospital.

Data and Code Availability

Data will be shared in accordance to NIH policy NOT-OD-21-013 (<https://grants.nih.gov/grants/guide/notice-files/NOT-OD-21-013.html>). We anticipate using the data for an open challenge prior to further sharing. The code for axon diameter imaging is available through Julia package `Microstructure.jl` (<https://github.com/Tinggong/Microstructure.jl>) and the code for myelin water imaging is available through Julia package `DECAES.jl` (<https://github.com/jondeuce/DECAES.jl>).

Author Contributions

Ting Gong: Conceptualization, Investigation, Methodology, Software, Visualization, Writing – original draft, Writing – review & editing. Chiara Maffei: Investigation, Writing – review & editing. Evan Dann: Investigation. Hong-Hsi Lee: Investigation, Writing – review & editing. Hansol Lee: Investigation, Writing – review & editing. Jean Augustinack: Resources, Writing – review & editing. Susie Y. Huang: Investigation, Resources, Writing – review & editing. Suzanne N. Haber: Investigation, Funding acquisition, Resources. Anastasia Yendiki: Conceptualization, Investigation, Funding acquisition, Resources, Supervision, Writing – review & editing

Declaration of Competing Interests

The authors declare that they have no known competing financial interests or personal relationships that could have appeared to influence the work reported in this paper. Anastasia Yendiki is a handling editor for *Imaging Neuroscience* and was not involved in the editorial review or the decision to publish this article.

Funding

This work was supported by the National Institute of Neurological Disorders and Stroke (R01-NS119911), the National Institute of Mental Health (R01-MH045573, P50-MH106435), and the National Institute of Biomedical Imaging and Bioengineering (R01-EB021265, U01-EB026996).

Supplementary materials

We saved complexed diffusion MRI and MSME data from one of the macaques for comparing the following denoising strategies.

- a. Directly denoise the magnitude data with MPPCA (Veraart et al., 2016b, 2016a).
- b. Denoising real-valued data. We retrieve the real-valued image data following the procedure described in (Eichner et al., 2015; Fan et al., 2020). The major implementation difference is that we apply 3D Fourier transformations and 3D Hanning windows as both our dMRI and MSME data are acquired using 3D imaging sequences. The imaginary part of the images containing purely noise is discarded while the real-valued images are assumed to contain only additive Gaussian noise and we further denoise them using MCPCA.
- c. Denoising complex data. We concatenate the real and imaginary parts of the complex images so that the data contains $2*N$ volumes (N is the number of DW measurements) and each volume contains Gaussian noise. We then estimate noise level and denoise the data using MPPCA. The denoised real and imaginary volumes are combined to magnitude data.

We compared the decay curve of denoised signals used for modelling. We use the direction-averaged signals versus b-values for diffusion MRI and the signals versus echo times for MSME data. Figure S1 shows the mean signal decay curves from small ROIs (9 voxels) in the splenium of corpus callosum. we didn't observe apparent differences of the decay curves from three denoising strategies. This suggests a relatively high SNR level in our ex vivo datasets compared to previous in vivo studies. Figure 2-3 further shows the denoised image maps from diffusion MRI and MSME. The difference between different denoising method can be visually seen from the background but not within the brain region.

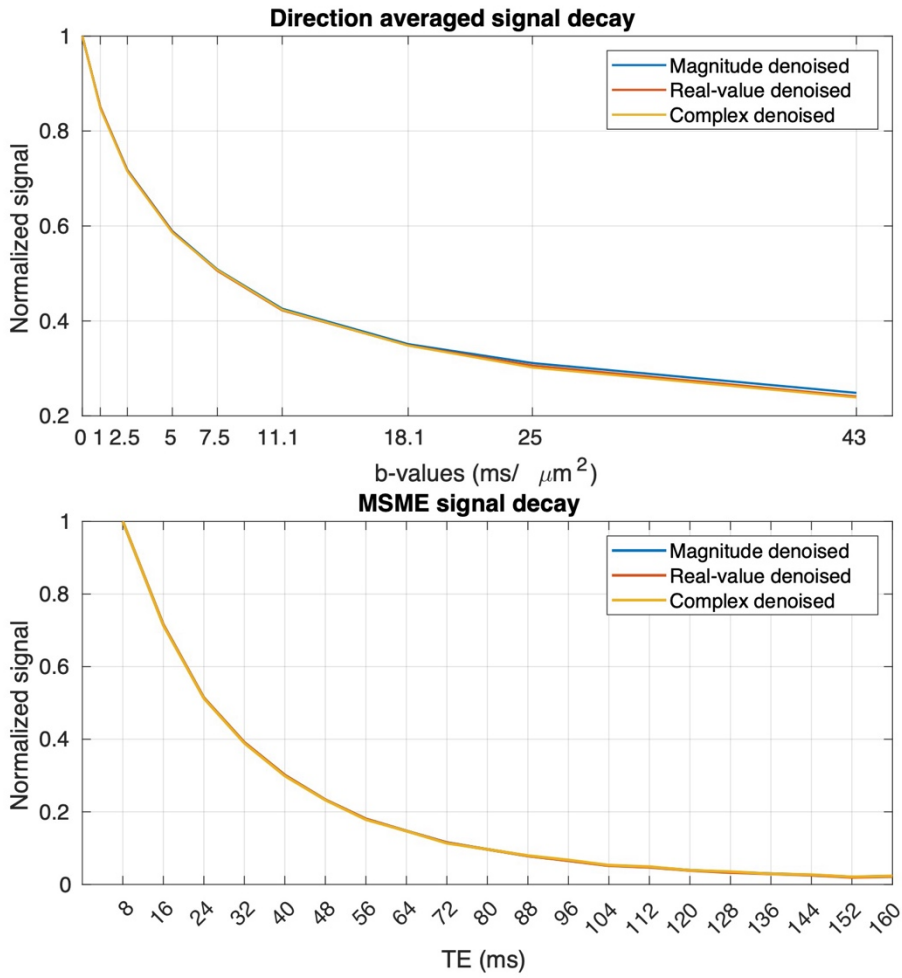


Figure S1. Signal decay curves of (a) direction-averaged dMRI signals and (b) MSME signals.

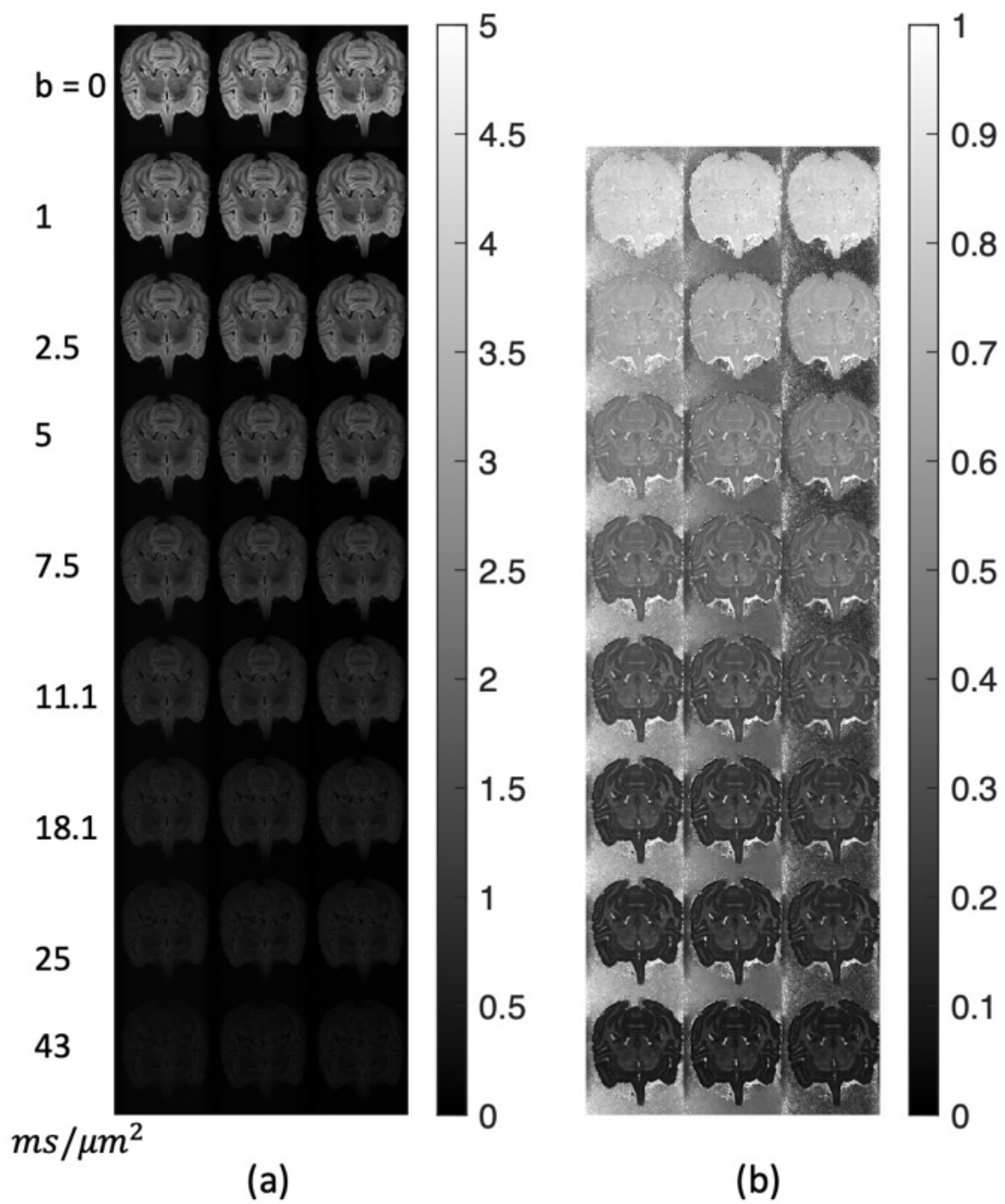


Figure S2. Direction-averaged images (a) and images after normalizing to $b=0$ (b). In (a) and (b), the first column shows magnitude denoised images, followed by real-value denoised and complex denoised images.

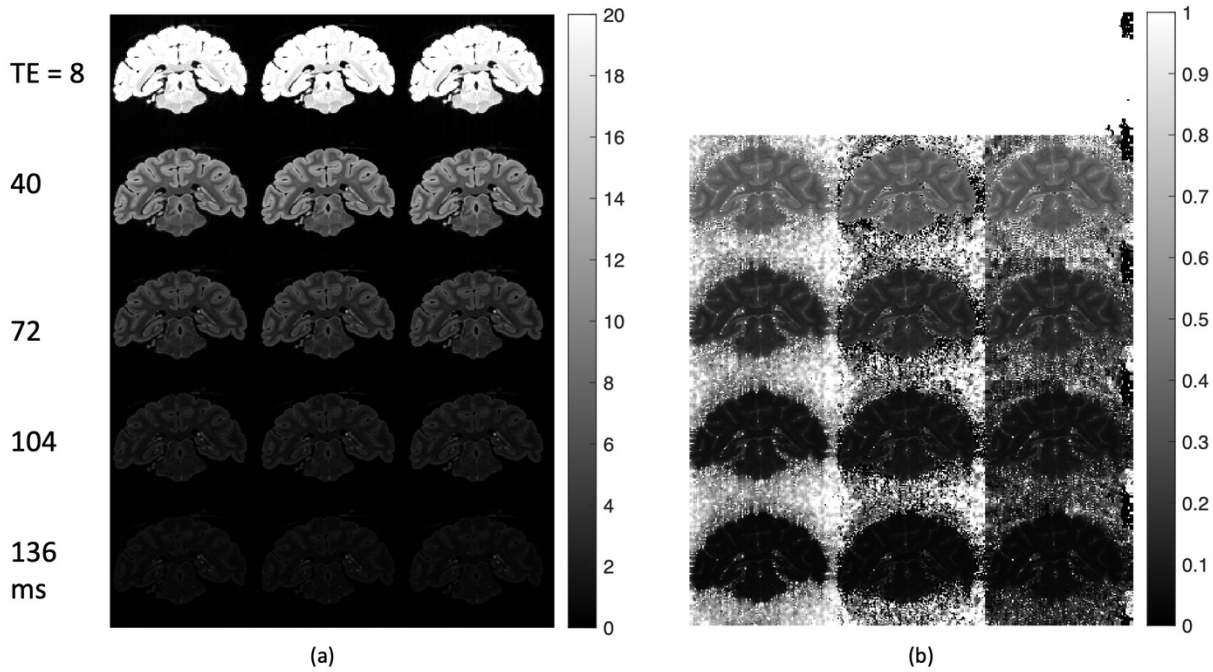


Figure S3. MSME images (a) and normalized MSME images (b) (normalized to images at shortest echo time (TE)). In (a) and (b), the first column shows magnitude denoised images, followed by real value denoised and complex denoised images.